# Alteration out of sight: a petrographic and HyLogger study of the McPhillamys gold deposit, east Lachlan Orogen, New South Wales

J. Fitzherbert, K. Hughes, K. Montgomery, P. Downes, C. Folkes, J. Egan, P. Flitcroft, S. Bodorkos & H. Huang

View supplementary material ⧉

Published online: 13 Jul 2025.

Submit your article to this journal ⧉

Article views: 430

View related articles ⧉

View Crossmark data ⧉

GEOLOGICAL SOCIETY OF AUSTRALIA Incorporated

Taylor & Francis
Taylor & Francis Group

🔓 OPEN ACCESS  |  Check for updates

# Alteration out of sight: a petrographic and HyLogger study of the McPhillamys gold deposit, east Lachlan Orogen, New South Wales

J. Fitzherbert[a] 🆔, K. Hughes[a], K. Montgomery[a], P. Downes[b] 🆔, C. Folkes[a] 🆔, J. Egan[c], P. Flitcroft[d], S. Bodorkos[e] 🆔 and H. Huang[f] 🆔

[a]Geological Survey of New South Wales, Maitland, Australia; [b]Perth, Australia; [c]Regis Resources LTD, Blayney, NSW, Australia; [d]Legacy Minerals, Orange, Australia; [e]Geoscience Australia, Canberra, ACT, Australia; [f]Advanced Analytical Centre, James Cook University, Townsville, QLD, Australia

### ABSTRACT

Lithology, alteration and Au mineralisation characteristics of the McPhillamys gold deposit in central NSW have proved difficult to interpret owing to structural overprinting. Previous models for the genesis of Au mineralisation include syngenetic (late Silurian Au-rich volcanic massive sulfide; VMS) or epigenetic (Carboniferous orogenic Au). We combine extensive new HyLogger spectral data (SWIR and TIR), petrographic analysis, geochronology and isotopic data to determine the alteration/mineralisation paragenesis, alteration zonation and effects of lithological control on mineralisation by using both downhole and broad-scale 3D mineralogical characterisation. The mineralisation at McPhillamys is stratabound within a coarse andesitic/dacitic volcaniclastic package. Alteration involved the development of an initial potassic core (microcline (ex-adularia)–quartz–pyrite) associated with the mineralised volcaniclastic package at the centre of the orebody and extending into the overlying non-mineralised andesitic volcanic/volcaniclastic package north and south of the mineralised zone. Propylitic-style alteration (albite–pyrite–chlorite–carbonate±epidote) forms an outer shell to the mineralisation, except at the northern and southern extents of the mineralised trend. White mica, chlorite, feldspar and carbonate all display consistent and mappable compositional variation between mineralised and non-mineralised sequences. It is difficult to decipher the early history of the deposit and geochronology (U–Pb and Ar–Ar), presented in this study, is unable to distinguish if mineralisation and alteration developed just after deposition of the host sequences during the latest Silurian (ca 423 Ma) with extensive recrystallisation during both Tabberabberan (ca 390 Ma) and Kanimblan (ca 350 Ma) orogenic events, or if mineralisation developed solely during the Tabberabberan Orogeny (ca 390 Ma) with extensive recrystallisation during the Kanimblan Orogeny (ca 350 Ma). We suggest the mineralogy, broad spatial distribution (700 m long, 250 m width, and up to 700 m depth) and paragenesis of alteration and mineralisation at McPhillamys are consistent with a deformed late Silurian lithologically controlled low-sulfidation epithermal, or potentially a shallow water (subsea-floor) Au-rich VMS system.

## Introduction

The McPhillamys Hill area has a long history of sporadic mining and exploration. Initial interest at McPhillamys focussed on the gold-bearing veins in the late 1880s (Roche, 1889) with modern exploration commencing in 1970 (French *et al.*, 2015). Several companies explored the area since, but it was not until 2006 that the Alkane Resources Ltd–Newmont Australia Ltd Joint Venture undertook shallow drilling and identified significant gold mineralisation over a 200 m by 450 m area (French *et al.*, 2015). Follow-up diamond drilling of this zone intersected multiple gold zones including 366 m @ 1.85 g/t Au starting from 134 m depth (Duerden, 2010). As at 2019, the McPhillamys project contained a resource totalling 69.8 million tonnes at

1.02 g/t with a contained proven and probable reserve of 60.8 million tonnes at 1.04 g/t (Regis Resources Ltd ASX announcement 19 July 2019).

The McPhillamys gold deposit has received limited research attention. Duerden (2010) described the main orebody as deformed stringer pyrite±chalcopyrite±pyrrhotite zone best developed in a package of coarse-grained volcaniclastic rocks with a narrow stratiform pyrite±sphalerite±galena zone overlying the main gold zone. Alteration includes a sericite±silica±carbonate±chlorite assemblage. Duerden (2010) proposed a late Silurian syngenetic control and favoured a Au-rich VMS model. Huston *et al.* (2016) published Pb isotopic data for McPhillamys that gave model ages overlapping with other late

This article has been corrected with minor changes. These changes do not impact the academic content of the article.

Silurian (*ca* 425 Ma) VMS deposits. French *et al.* (2015, 2017) described the gold mineralisation as associated with a quartz + carbonate (ankerite) + white mica (phengite) + pyrite ± chalcopyrite ± pyrrhotite ± sphalerite ± galena ± arsenopyrite ± biotite assemblage within a coarse-grained volcaniclastic-rich sequence. Those authors concluded that gold mineralisation developed under greenschist facies metamorphic conditions during the Carboniferous Kanimblan Orogeny that also produced the metamorphic mineral assemblage of biotite, chlorite, muscovite, quartz and K-feldspar.

In this study, we characterise the otherwise cryptic alteration and mineralisation features at McPhillamys through systematic petrographic and 3D hyperspectral analysis of drill core and present new dating (U–Pb zircon and titanite and Ar–Ar white mica) and sulfur-isotope results.

## Geological setting

The McPhillamys deposit is hosted by the late Silurian Anson Formation, which is located towards the base of the Mumbil Group in the eastern Lachlan Orogen of New South Wales (Figure 1). This formation overlies basaltic andesite to basaltic volcanic/volcaniclastic sequences of the Ordovician Blayney Volcanics and is conformably overlain by the Lower Devonian Mullions Range Volcanics (Pogson & Watkins, 1998). Deposition of the Mumbil Group commenced in the early late Silurian with shallow marine, shelf sedimentation (Mumbil Shelf) developed on the Molong High along the western flank of the developing deep water Hill End Trough (HET). The HET opened as one of series of troughs or basins developed in a wide back-arc setting behind a west-dipping subduction zone outboard of the east Gondwana margin (Collins, 2002).

The HET and Mumbil Shelf sequences experienced two major phases of east–west shortening. Initial inversion of the HET and flanking shelves occurred during the Middle Devonian Tabberabberan Orogeny, with a second phase of deformation during the Carboniferous Kanimblan Orogeny (Glen & Watkins, 1999). There is conjecture over the importance of these two deformation events. Powell (1976) and Powell and Edgecombe (1978) suggest that Tabberabberan deformation was weak, and most of the east–west shortening of the HET occurred during the Kanimblan Orogeny. More recently, Fergusson and Colquhoun (2021) suggested that regional east–west shortening of the HET was of latest Devonian to early Carboniferous age (*i.e.* post-Tabberabberan Orogeny). Conversely Glen and Watkins (1994, 1999), Pogson and Watkins (1998), and Packham (1999) contend that the Tabberabberan Orogeny was the main inversion phase of the HET.

The Anson Formation at McPhillamys is deformed with a schistose foliation developed and is locally pervasively altered, making protolith determination difficult. Duerden (2010) and French *et al.* (2017) summarise the general characteristics of the lithological sequence at McPhillamys as comprising a basal polymict conglomerate rich in clasts of limestone, porphyry, siltstone and mudstone that grade into a thinly-bedded to laminated sequence of calcareous siltstone and mudstone, with

thicker-bedded, massive fossiliferous limestone intervals (Figure 2a). The calcareous beds are overlain by a sequence of andesitic to dacitic, medium- to coarse-grained volcaniclastic (Figure 2b) and coherent volcanics (Figure 2c). Narrow (~2 m) intervals of a feldspar–phyric dacite dykes or sills have also been intersected (Figure 2d). The andesitic to dacitic volcanics/volcaniclastics are extensively altered (see below) and host the gold mineralisation. Weakly to unaltered overlying sequences comprise fine- to medium-grained intermediate volcaniclastic rocks and minor shale with minor stratiform pyrite–sphalerite–galena mineralisation (Duerden, 2010).

Volcanic and volcaniclastic rocks of the Anson Formation are underlain by a fossiliferous limestone member, containing Ludlow-aged faunal assemblages (Pogson & Watkins, 1998) corresponding to the interval 427–423 Ma. A rhyolite of the overlying Mullions Range Volcanics has a U–Pb sensitive high-resolution ion microprobe (SHRIMP) age of 417 ± 4 Ma (Black in Pogson & Watkins, 1998).

Mineralisation at McPhillamys forms a flattened conical zone of stringer and disseminated pyrite/gold over 700 m long, 250 m width and up to 700 m in depth (Figure 1, Inset 1). It is developed within the medium- to coarse-grained (up to cobble conglomerate) andesitic to dacitic volcaniclastic and coherent volcanics. The mineralisation is located on a series of north–south-trending dextral splays of the NNW-trending Godolphin Fault (French *et al.*, 2017). Movement on these structures is responsible for greenschist facies shearing in the Anson Formation. One structure previously interpreted to be associated with the deposit is the informally named Sherlock fault. This structure has been interpreted to separate the non-mineralised footwall from the mineralised zone (coincident with significant changes in the alteration mineralogy).

## Sampling and analytical methods

Eleven diamond drillholes were selected for hyperspectral scanning with 110 thin-sections cut from intervals along the length of six holes (RRLMPDD066, RRLMPDD0127, RRLMPDD0139, RRLMPDD0205, RRLMPDD0214 and RRLMPDD0218; Figure 1, Inset 1). The thin-section study focussed on alteration mineralogy, paragenesis and texture and confirmation of hyperspectral data.

Core from the diamond drillholes was scanned using GSNSW's HyLogger based at the W.B. Clarke Geoscience Centre, Londonderry NSW. The HyLogger 3 system automatically collects hyperspectral data and high-resolution core imagery along the length of drillhole. For a description of the HyLogger system used in this study, refer to Downes *et al.* (2016) and Schodlok *et al.* (2016). TSG (The Spectral Geologist) software was then used to analyse the spectral reflectance data. A discussion of the specialised TSG scalars that were applied to the spectral datasets is included in the supplemental data. Lithology, hyperspectral data and assays were plotted in Golden Softwares' Strater software, with data down-sampled to 1 m averages to ensure easy viewing for characterisation.
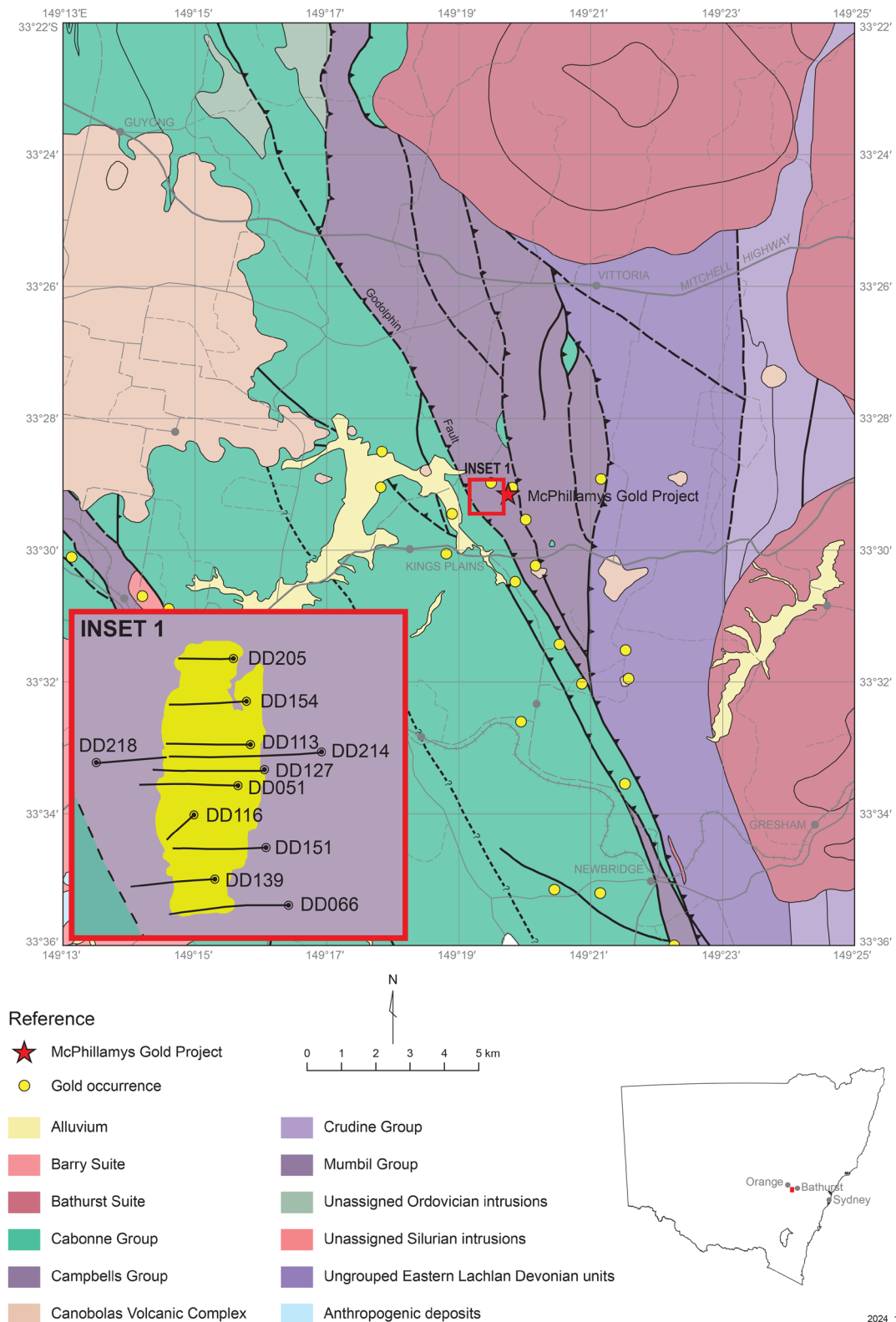
**Figure 1.** Geological map showing major tectonostratigraphic units and location of the McPhillamys deposit and nearby prospects with respect to the Godolphin Fault. The extent of mapped rock units and fault locations are from the NSW Seamless Geology dataset (Colquhoun *et al.*, 2025). Inset 1 represents the maximum extent of Au mineralisation at McPhillamys (as modelled in this study) projected to surface (yellow polygon) overlain by the collars and surface projected traces of all drill holes used in this study; all drill hole labels are missing the prefix RRLPM.

Numerical 3D modelling of the interpreted mineral abundance data merged with gold abundance data was carried out using Seequent's Leapfrog Geo software. Mineral species identified in the SWIR and TIR datasets, using TSG software, were exported using 1 m downhole bins and imported into the Leapfrog Geo software. Models were produced using a spherical

**Figure 2.** Photographic montage showing typical lithologies encountered in drill core from the McPhillamys deposit. (a) Typical recrystallised limestone from the lower calcareous package (drillhole RRLMPDD218～304 m; note the abundant pink Mn carbonate). (b) Coarse-grained (conglomerate) volcaniclastic with deformed elongate andesitic clasts from the upper coarse-grained volcaniclastic package (drillhole RRLPMDD066～272 m). (c) Coherent andesitic volcanic from the upper andesitic volcaniclastic/volcanic package. The cross-cutting vein comprises bladed carbonate, quartz and epidote with chlorite (drillhole RRLMPDD214～194 m). (d) Narrow holocrystalline to feldspar-pyric dacite interval (drillhole RRLMPDD214～197 m).

interpolant with no regional trends. In addition, a gold occurrence model was constructed in the 3D workspace using a low-grade gold cutoff value of 0.01 g/t Au. The gold model was constructed using assay and lithological data from 362 drill holes; we note that this is not a robust gold resource model but illustrates the main mineral and geochemical relationships identified in this study; details of the modelling are included in the supplemental data. Multiple variations were modelled for each alteration mineral by using different parameters such as down-hole compositing to find the best fit for each data set. In many cases, only minimal changes to the broad trends were observed between iterations. Alteration-related minerals, including white mica, feldspar, chlorite, and carbonate were identified in the logging and interpreted mineral data, and each mineral was modelled separately.

Geochronological studies were carried out on zircon, titanite and muscovite. Details are included in the supplemental data and results discussed below. Zircon from a gold mineralised, altered and sheared intermediate volcaniclastic rock at McPhillamys (drillhole RRLMPDD216) were separated for U–Pb

SHRIMP analysis at Geoscience Australia. The volcaniclastic rock was pyrite-rich (~3 wt%) and required dissolution of the pyrite using concentrated nitric acid to access zircon. Eight zircon grains were recovered.

Laser ablation inductively coupled plasma mass spectrometry (LA-ICP-MS) U–Pb titanate dating and Ar–Ar white mica dating were carried out on mineralised samples. Dating of titanite at James Cook University proved challenging owing to its inclusion-rich nature, fine grainsize and low abundance in the samples. Two titanite samples were analysed. Titanite from a volcaniclastic rock, sample McPhil01 (drillhole RRLMPD066, 333.1–333.4 m depth) is intergrown with and forms rims around cubic pyrite. The second titanite sample (McPhil02, drillhole RRLMPDD214, 290.5–290.7 m depth) was intergrown with cubic pyrite within a quartz vein from the hanging wall to mineralisation. Muscovite laths from a foliated pyrite–muscovite–quartz-rich zone with relic feldspar (McPhil03, drillhole MPRCD015 509.35–510.45 m depth) were step-heated in 12 steps for $^{40}Ar/^{39}Ar$ analyses at the University of Melbourne.

**Table 1.** Sulfur-isotope data for sulfides from the McPhillamys deposit.

| Sample location (drillhole prefix = RRLMP | Pyrite ($\delta^{34}S$‰ VCDT) | Chalcopyrite ($\delta^{34}S$‰ VCDT) | Galena ($\delta^{34}S$‰ VCDT) | Sphalerite ($\delta^{34}S$‰ VCDT) |
|---|---|---|---|---|
| DD034 252 m | 5.2 | | | |
| DD062 120.25–120.5 m | −15.0 | | −0.9 | 1 |
| DD066 202.36 m | 7.0 | | 5 | |
| DD079 230.2 m | | | | 1.4 |
| DDW068 219.83 m | 2.6 | | 2 | 2.7 |
| RCD015 481.5 m | 1.5 | | | |
| RCD015 509.35–510.45 m | 0.9 | 0.8 | | |
| RCD019 171.55 m | 1.7 | 1.6 | | |
| RCD019 175.25 m | 1.6 | | | |
| RCD019 195.7 m | 0.9 | | | |
| RCD019 261 m | 1.2 | | | |
| RCD019 261 m | 22.6 | | | |
| RCD019 282.35 m | | 0.8 | | |
| RCD019 292.9 m | | 0.7 | | |
| RCD019 343.15 m | 1.5 | | | |
| RCD019 348.6 m | 0.7 | 0.1 | | |
| RCD019 351 m | | 1.6 | | |
| RCD019 455.4 m | 2.1 | | | |
| RCD019 460.4 m | 2.0 | | | |
| RCD024W 354.5 m | 1.5 | | | 2.2 |

Four high-precision lead isotope analyses for galena from McPhillamys were reported in Huston *et al*. (2016). The data were modelled for their estimated lead model ages—the age of extraction of lead from the lead reservoir by using the unpublished calculator developed by David Champion and David Huston of Geoscience Australia (see Huston *et al*., 2017).

Twenty-nine sulfur-isotope analyses were carried out at the Nevada Stable Isotope Laboratory, University of Nevada, Reno, USA. Details of the analytical method, sample locations and results are included in the supplemental data, summarised in Table 1 and discussed below.

## Results

### *Petrographic characteristics of alteration*

#### *Alteration mineralogy, paragenesis and texture*
Alteration at McPhillamys is extensive and centred around a broad, flattened conical-shaped potassic core (~600 m × 400 m) characterised by a K-feldspar (microcline)–white mica–pyrite–quartz ± carbonate–biotite assemblage. This potassic core is flanked by a propylitic halo characterised by albite–chlorite–carbonate–pyrite ± epidote–biotite–magnetite–actinolite–pyrite assemblage. The alteration is concentrated within the andesitic/dacitic volcaniclastic and coherent volcanic facies. It has a similar expression in both units but is typically less well developed in the coherent volcanic packages. A zone of high strain overprints and post-dates the mineralisation/alteration. This deformation recrystallised and modified the host rock and altered/mineralised regions and is responsible for the development of schistose fabrics. Figures 2–4 illustrate examples of the textures, alteration assemblages and rock types discussed below.

Within the potassic core, porphyritic volcaniclastic/coherent volcanic sequences have undergone an initial potassic (K-feldspar—formerly adularia, now microcline) alteration that is overprinted by a pervasive sericitic white mica assemblage. In zones of low strain, K-feldspar is associated with pyrite–quartz ± carbonate–biotite veins. Narrow zones (up to 10 mm wide) of intense K-feldspar alteration resulting in the textural destruction of the host rock occur adjacent to larger pyritic veins and in zones of abundant small-scale pyritic veining (Figure 3a, b). The potassic alteration is still pervasive away from the zones of textural destruction where it is associated with abundant disseminated pyrite, but the porphyritic nature of the primary rock type is preserved (Figure 3c, d). Carbonate occurred late in the vein history, commonly infilling the centre of K-feldspar-rich veins, but is also studded throughout the host sequences. Sub-rhombic pseudo-acicular adularia (or microcline after) is rarely preserved in veins (Figure 3e) and more commonly as interlocking sub-rhombic forms as a replacement after volcanic rock phenocrysts (Figure 3d). The initial potassic alteration is overprinted by a sericitic white mica (generally after K-feldspar or albite) ± chlorite (after biotite) assemblage (Figure 3f, g). In zones of low strain, this phyllic-style alteration is focussed in the matrix to coarse volcaniclastic rocks along with pyrite and is pervasive throughout finer-grained volcaniclastic and coherent lithologies.

Propylitic alteration surrounds the potassic alteration zone and displays varying mineralogical features between the hanging wall to mineralisation when compared with the mineralised interval and the footwall to mineralisation. Better textural preservation of coherent volcanic rocks is common, particularly in the hanging wall, and although phenocrysts are replaced by secondary mineralogy, grain shapes are preserved (Figure 4b); veining associated with alteration is also better preserved within this zone (Figure 2c). Propylitic alteration in the hanging wall to mineralisation (*e.g.* drillhole RRLMPDD0214) is characterised by carbonate–epidote–chlorite–quartz ± actinolite veins that are associated with albite–carbonate–chlorite–quartz ± epidote (±biotite) alteration of the volcanic host rocks (Figure 4a–c). Sericitic white mica can be abundant, commonly in strongly sheared zones. Propylitic alteration towards the southern and northern ends of the orebody is host to moderate Au mineralisation. At the southern end of the orebody, propylitic alteration is characterised by deep-red, jasperoidal crustiform, colloform to comb textured veins that commonly comprise delicate oscillating intergrowths of hematite within dog-tooth carbonate, surrounded by colloform-banded carbonate and Mn-enriched carbonate cores (Figure 4e, f). The host-rock alteration associated with the veins is a mix of deep-green chlorite (some biotite is present in vein selvages), carbonate (commonly Mn-enriched), albite, pyrite and sericitic white mica with some magnetite. In most cases, this propylitic mineral assemblage is continuous into the calcareous beds that underly the volcanic sequences. At the northern end of the orebody, the Au mineralisation occurs in the footwall to the potassic alteration zone, and here the volcanic host rocks are crosscut by felted, vuggy to dog-tooth carbonate–quartz ± pyrite veins. In zones of low strain, the porphyritic texture of the host andesitic volcanics is preserved with albite-replaced plagioclase phenocrysts, while the matrix is extensively overprinted by carbonate spotting, chlorite and sericitic white mica. Where white mica is present, the andesite is strongly sheared, forming white mica–chlorite–carbonate–pyrite schist.
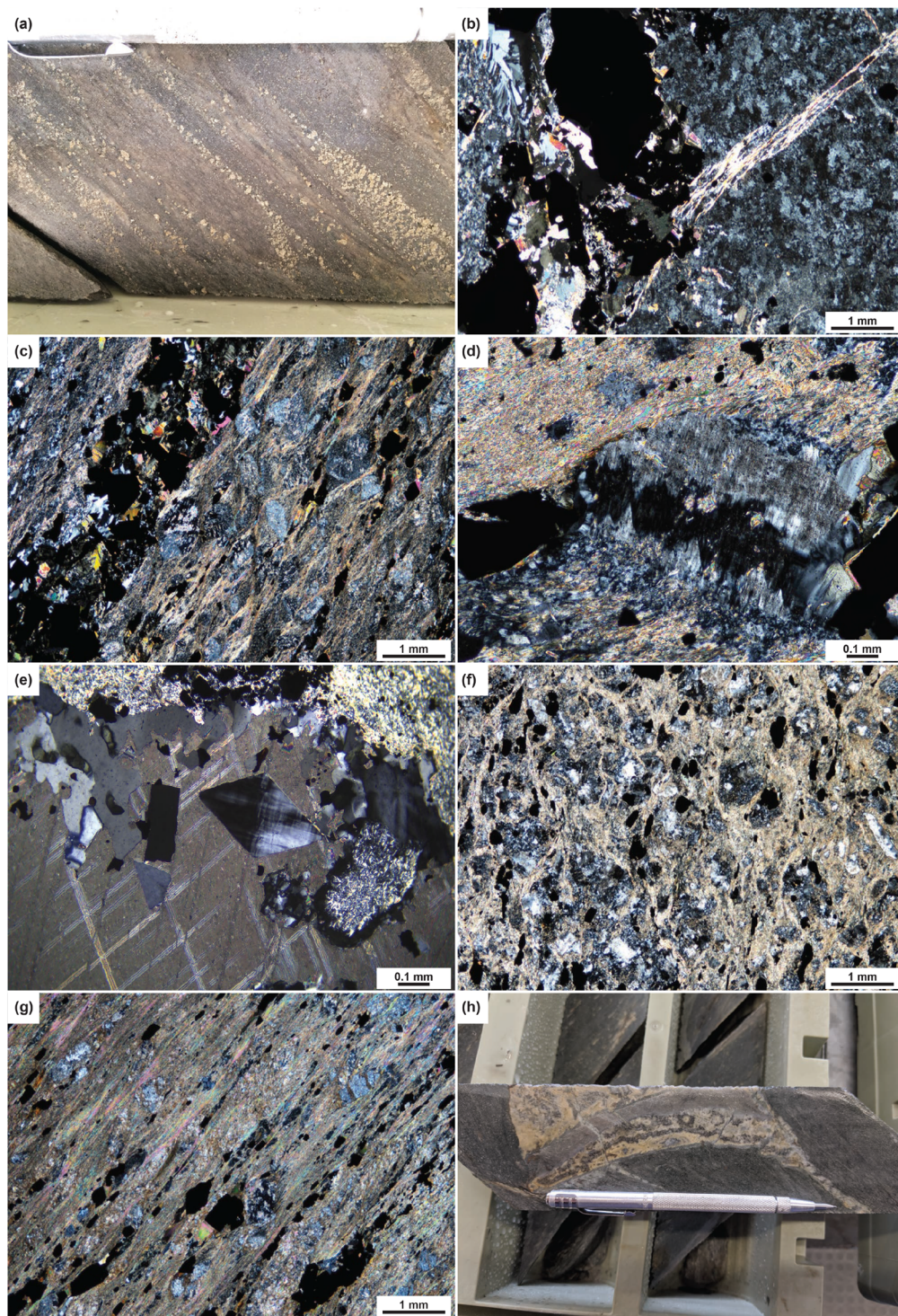
**Figure 3.** Photographic montage showing typical mineralogy and textures of the potassic-altered rocks. (a) Deformed stringer pyrite–quartz–K-feldspar (adularia) veins within an extensively K-feldspar altered volcaniclastic (drillhole RRLMPDD127, ~262 m). (b) Cross-polarised light image illustrating pyrite–quartz–white mica–carbonate stringer vein surrounded by a selvage of intense K-feldspar alteration that has resulted in textural destruction of the porphyritic host (drillhole RRLMPDD127, ~270 m). (c) Cross-polarised light image illustrating strongly deformed, K-feldspar and white mica altered porphyritic andesitic volcaniclastic adjacent to a pyrite–white mica–carbonate stringer vein—all phenocrysts are replaced by composite K-feldspar (note the schistose foliation developed in the host) (drillhole RRLMPDD127, ~266 m). (d) Cross-polarised light image illustrating adularia (now microcline) replacing a plagioclase phenocryst within altered andesitic host rock—note the partial replacement within the enveloping white mica defined foliation (drillhole RRLMPDD127, ~290 m). (e) Cross-polarised light image illustrating well preserved rhombohedral adularia preserved within a boudinage vein clast—note the weak development of tartan twinning owing to deformation (drillhole RRLMPDD0127 ~281 m). (f) Cross-polarised light image illustrating pervasive white mica replacement of the K-feldspar altered host rock within a low strain zone. (g) Cross-polarised light image illustrating typical intensely deformed white mica (phengite) and pyrite replacing andesitic host rock—some K-feldspar-replaced phenocrysts are still preserved (drillhole RRLMPDD127, ~270 m). (h) Boudinaged fragment of a crustiform banded quartz–siderite–adularia vein with a probable (now recrystallised) chalcedonic core (drillhole RRLMPDD205, ~154 m).
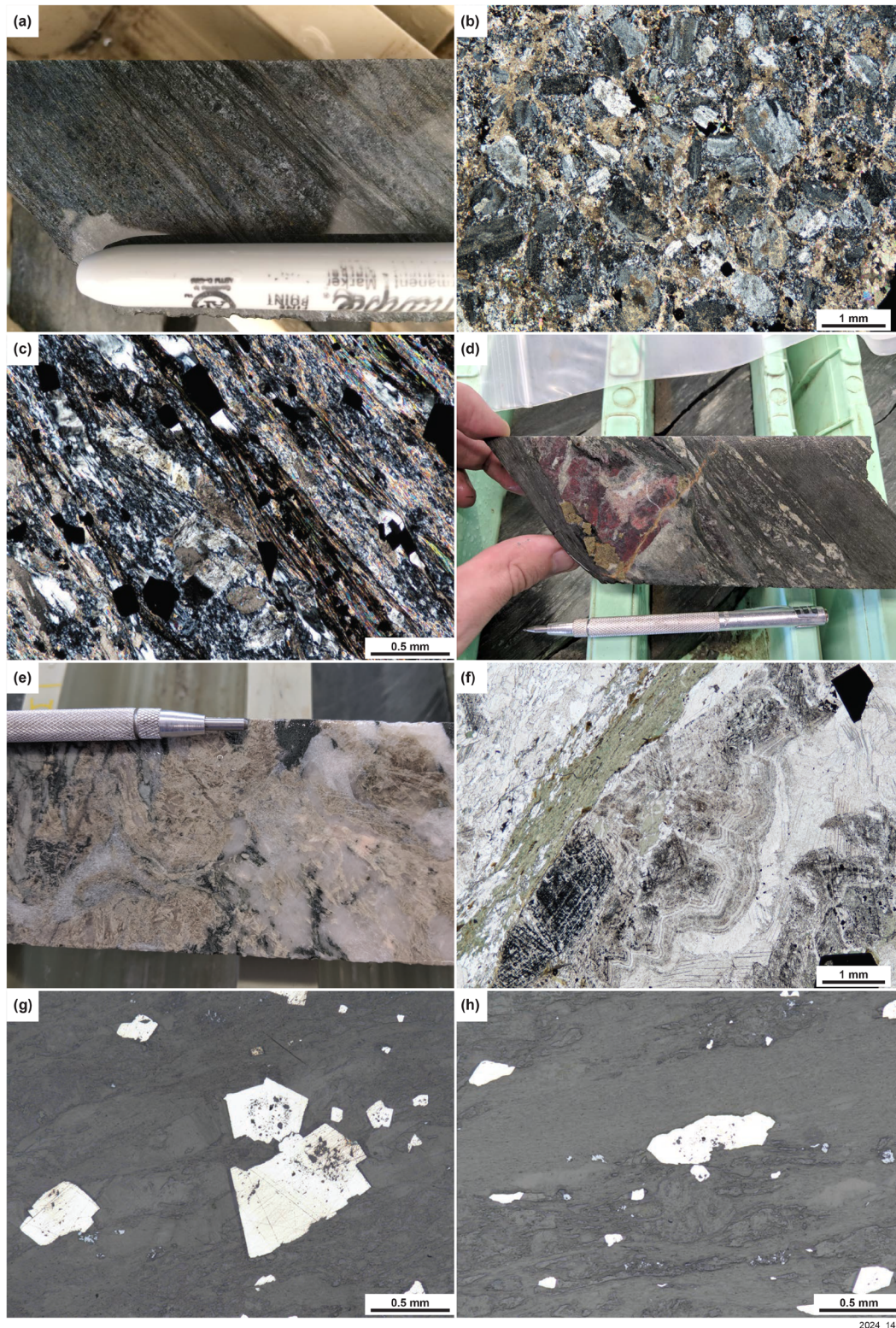
**Figure 4.** Photographic montage showing typical mineralogy and textures of the propylitic-altered zone. (a) Strongly deformed chlorite, albite, pyrite, carbonate (calcite and Mn carbonate), white mica altered andesitic volcaniclastic (drillhole RRLMPDD127, ~459 m). (b) Cross-polarised light image illustrating a relatively low strain albite–carbonate–chlorite altered coherent andesite clast (drillhole RRLMPDD066 ~ 571 m). (c) Cross-polarised light image illustrating the intensely porphyro-clastic remnants of the propylitic-altered andesite host (lower centre of photograph; drillhole RRLMPDD127, ~485 m). (d) Boudinage fragment of a jasperoidal (hema-tite dusted quartz vein with a pink Mn carbonate core—note the delicate crustiform texture in the top left of the vein (drillhole RRLMPDD066, ~570 m). (e) Bladed carbonate vein displaying partial silica replacement (drillhole RRLMPDD214, ~237 m). (f) Plane-polarised light image illustrating the delicate crustifrom/coliform texture of a quartz–hematite–carbonate (Mn carbonate and calcite) vein—note the schistose foliation enveloping the vein fragment (drillhole RRLMPDD066, ~466 m). (g) Reflected light image illustrating sieved, silicate inclusion-rich dodecahedral $pyrite_1$ cores surrounded by euhedral cubic $pyrite_2$ rims (drillhole RRLMPDD127, ~362 m). (h) Reflected light image illustrating a lozenge-shaped (resorbed) pyrite—note the partial preservation of the silicate inclusion-rich $pyrite_1$ core and development of inclusion-free $pyrite_2$ within the pressure shadows (drillhole RRLMPDD127, ~362 m).

### Ore mineralogy, paragenesis and texture

Pyrite–Au mineralisation broadly coincides with the potassic core of the orebody but transgresses and extends into the porphyritic halo to the north and south. The main form of mineralisation involves deformed quartz and As-enriched pyrite (up to 1 wt% As; Fitzherbert *et al*., 2024) in stringers and in the matrix to clastic/pseudoclastic breccias (Figure 3a–c). Pyrite is the host to Au mineralisation, but minor pyrrhotite, chalcopyrite, chalcocite, sphalerite and rare galena are also present. The mineralised interval is strongly sheared, and pyrite is multiphase (Figure 4g, h). Pyrite$_1$ cores are Au(As)-enriched (refractory within pyrite), sub-rounded in form and sieved with silicate inclusions (Figure 4g; Fitzherbert *et al*., 2024). Sulfide bleach etching reveals pyrite$_1$ cores are oscillatory zoned with a pyritohedron form (Fitzherbert *et al*., 2024). Pyrite$_1$ cores are overgrown by Au-barren and As-poor, massive, inclusion-poor rims (pyrite$_2$) that are cubic in form (Figure 4g; Fitzherbert *et al*., 2024). Chemical mapping of pyrite grains reveals that both pyrite$_1$ cores and pyrite$_2$ rims display evidence of chemical modification owing to strain induced element diffusion, with many grains displaying a distinctive lozenge shape owing to recrystallisation to pyrite$_3$ (with reduced Co and Ni) within the penetrative foliation (Figure 4h; Fitzherbert *et al*., 2024; Pal *et al*., 2009).

Vein fragments preserved in low-strain windows display a range of textures, including (i) crustiform and coliform banding (Figures 3h and 4d, f); (ii) chalcedonic quartz and carbonate veins within the potassic-altered zone; and (iii) coliform quartz, Mn carbonate as well as hematite veins preserved in the propylitic footwall (Figure 4d). Bladed calcite ± epidote veins also occur in the hanging wall andesitic volcanics, with the bladed carbonate locally displaying silica replacement (Figure 4e).

### Hyperspectral logging

#### HyLogger determined stratigraphy

Field-based lithological logging at McPhillamys has proven difficult and was not recorded beyond the identification of a lower calcareous package and an overlying variably mineralised volcaniclastic and lava package (*e.g.* French *et al*., 2017, figure 2). The hyperspectral data presented in this study display variability in the alteration mineralogy that is controlled by lithological variation and can be correlated along the length of the orebody (Figure 5). A full stratigraphic section from hanging wall through to footwall was constructed using data from drillholes RRLMPDD051, RRLMPDD127 and RRLMPDD214. This can be correlated in drill cores to the north and south. From base to top, the sequence includes:

- a basal calcareous package;
- a lower coarse volcaniclastic package enriched in chlorite, albite and carbonate with moderate quartz that has aspectral domains of interbedded siltstone;
- a finer-grained feldspar-poor volcaniclastic package that grades upwards into an upper coarse volcaniclastic package with increased chlorite, carbonate and feldspar; and

- an andesitic volcanic/volcaniclastic package dominate by chlorite, carbonate and feldspar.

An identical but compressed sequence is also present in drillhole RRLMPDD066 in the south of the orebody, while in the north part of the orebody, drilling intersected stratigraphy most consistent with the upper and lower volcaniclastic packages and into the andesitic lava package at the top of drillhole RRLMPDD205 (Figure 5).

#### HyLogger-determined alteration mineralogy

The HyLogger-determined mineralogical characteristics of alteration at McPhillamys are summarised below in three east-to-west cross-sections (see Figure 1 Inset 1) through the southern (drillhole RRLMPDD0066; Figure 6), central (drillholes RRLMPDD127 and RRLMPDD214; Figure 7a, b) and northern (drillholes RRLMPDD154 and RRLMPDD205; Figure 8a, b) parts of the mineralised body (see the supplemental data for lithological and spectral summary figures for the remaining six drillholes). The distribution of minerals identified in the spectral datasets for these three cross-sections is summarised below in terms of variation in mineralogy/spectral response in the hanging wall to mineralisation, within the mineralised interval, and within the footwall to mineralisation zones. Importantly, there is no primary mineralogy preserved in the host lithologies at McPhillamys, and the mineralogy interpreted from the spectral data is related to alteration, albeit with variations related to the previously defined primary rock types. All discussion of variable mineral species or general compositional groups [*e.g.* white mica (phengite–muscovite), chlorite (Fe-chlorite, Fe–Mg-chlorite, Mg-chlorite), feldspar (*e.g.* albite, K-feldspar)] is based on the standard TSG (8.1.05, May 2022) mineral classification algorithms, with the exception of carbonate species, which were classified in accordance with Green and Schodlok (2016) and further documented in Hughes and Fitzherbert (2025).

***Southern section.*** Gold mineralisation in drillhole RRLMPDD0066 (Figure 6) is continuous from ~310 m to 625 m and is hosted within both the upper and lower coarse volcaniclastic packages, with the highest grades commonly corresponding to volcaniclastic conglomerate units. This is the only drillhole where mineralisation is present in the lower, coarse volcaniclastic package.

The alteration mineralogy of the hanging wall to mineralisation displays variability that generally correlates with logged lithological variation. Intervals of volcaniclastic comprise abundant chlorite with lesser white mica and carbonate, as well as abundant plagioclase (albite), with K-feldspar and very low modal quartz. Intervals that host finer-grained lithologies typically have more abundant white mica, lower modal chlorite and more abundant carbonate, with increased quartz and decreased plagioclase (albite). K-feldspar is typically in very low abundance or absent from these finer-grained intervals. Chlorite within volcaniclastic lithologies is predominantly mixed Fe–Mg and Fe-rich variants with a relatively narrow composition (chlorite wavelength ~2256 nm), although there is greater variability
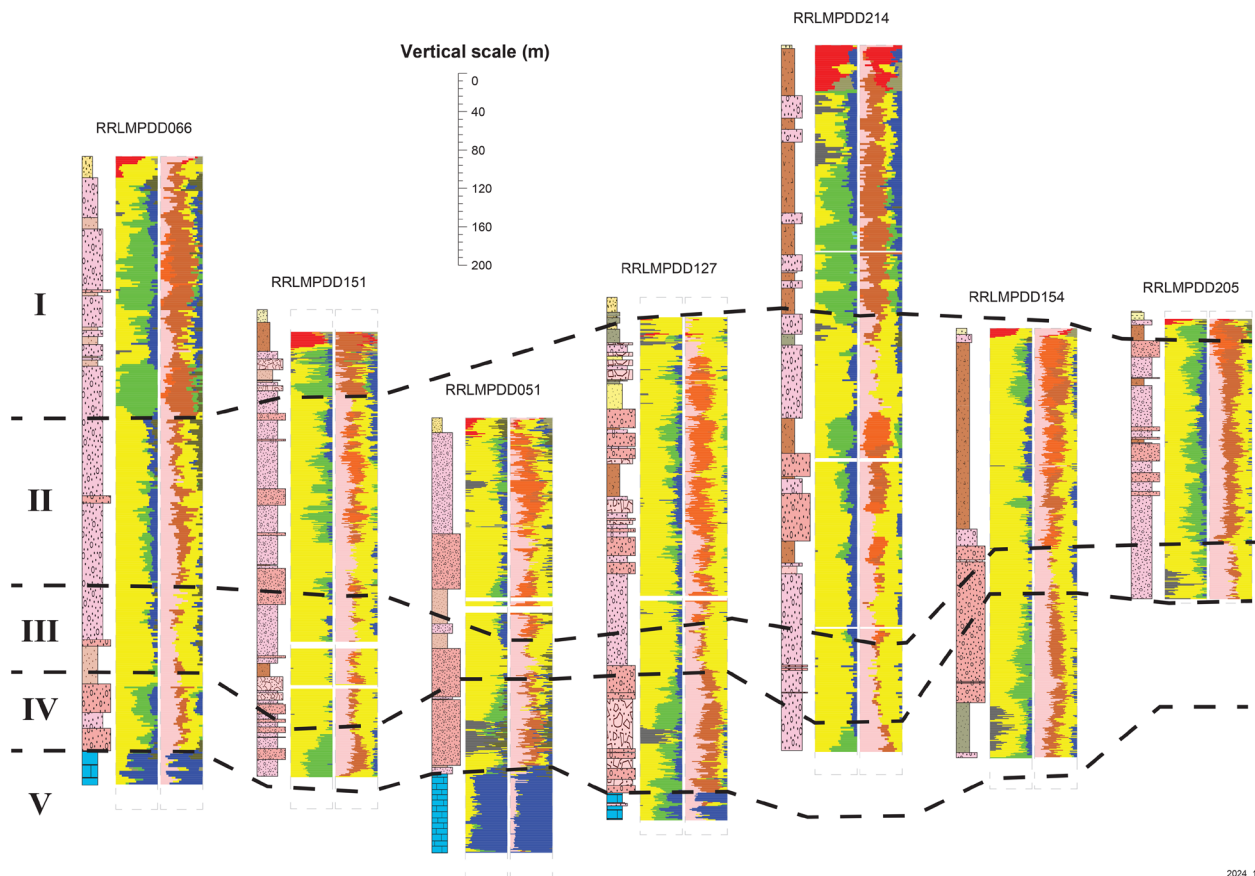
**Figure 5.** Hyperspectral and lithological-based stratigraphic correlation within the McPhillamys orebody based on selected TSG logs. All logs comprise from left to right, a company lithological log, HyLogger SWIR output, and HyLogger TIR output (complete lithological and hyperspectral logs for all drillholes used in this study can be found in the supplemental data). The lithological subdivisions separated by dashed lines are: I, andesitic volcanic/volcaniclastic package; II, upper coarse volcaniclastic package; III, feldspar-poor volcaniclastic package; IV, lower coarse volcaniclastic package; and V, basal calcareous package.

around logged finer-grained intervals (chlorite wavelength 2240–2256 nm). White mica is phengitic (Al–OH wavelength 2216–2219 nm). Carbonate in the hanging wall is a mix of calcite and kutnohorite, with some ankerite also present in the finer-grained volcaniclastic intervals between 140 and 210 m.

The mineralised interval displays an overall lower chlorite abundance and increased white mica, with a decrease in plagioclase (albite) and a correlative increase in quartz compared with the hanging wall sequence. K-feldspar is absent. Where present, chlorite is Fe-enriched with a narrow compositional range and only a minor shift to shorter wavelengths (2248–2252 nm) compared with chlorite in the hanging wall. White mica is mostly phengitic but displays a constant shift to shorter Al–OH feature wavelengths (2208 nm) towards the base of the upper coarse-grained volcaniclastic package; this wavelength shift likely reflects unlogged lithological variation. Carbonate in the mineralised interval grades from a narrow upper interval with minor calcite, which is underlain by a fine-grained feldspar-poor volcaniclastic that hosts ankerite and minor kutnohorite. Only minor calcite with lesser kutnohorite occurs in the lower coarse-grained volcaniclastic package at the base of the mineralised interval.

Calcareous metasedimentary sequences form the footwall to mineralisation in this section comprise white mica and minor

chlorite, with abundant carbonate and quartz. Chlorite in this domain is a mix of Fe–Mg- and lesser Fe-rich compositions, with a narrow compositional range (~2252 nm). White mica is phengitic with a small shift to shorter Al–OH wavelength ~2214 nm while the carbonate is dominated by calcite.

***Central section.*** Gold mineralisation in hole RRLMPDD0127 is continuous from ~50 m to 410 m, while hole RRLMPDD0214 was drilled from further east into the hanging wall sequences and intersected mineralisation below RRLMPDD0127 at depths of ~440–670 m. In both holes, the mineralisation is hosted within the upper, coarse volcaniclastic package.

Hanging wall alteration is best represented in hole RRLMPDD0214 (Figure 7b). Here, the alteration response is consistent with variability that correlates with logged lithology. Logged intervals of intermediate extrusive rocks (andesitic lava/volcaniclastic package) comprise chlorite, plagioclase (albite), carbonate ± white mica with minor epidote and relatively low quartz abundance. Conversely, volcaniclastic intervals in the hanging wall are characteristically enriched in white mica and quartz, and display variable carbonate abundance with chlorite and plagioclase typically less abundant or absent. Where present, chlorite is predominantly a mixed Fe–Mg variant with lesser
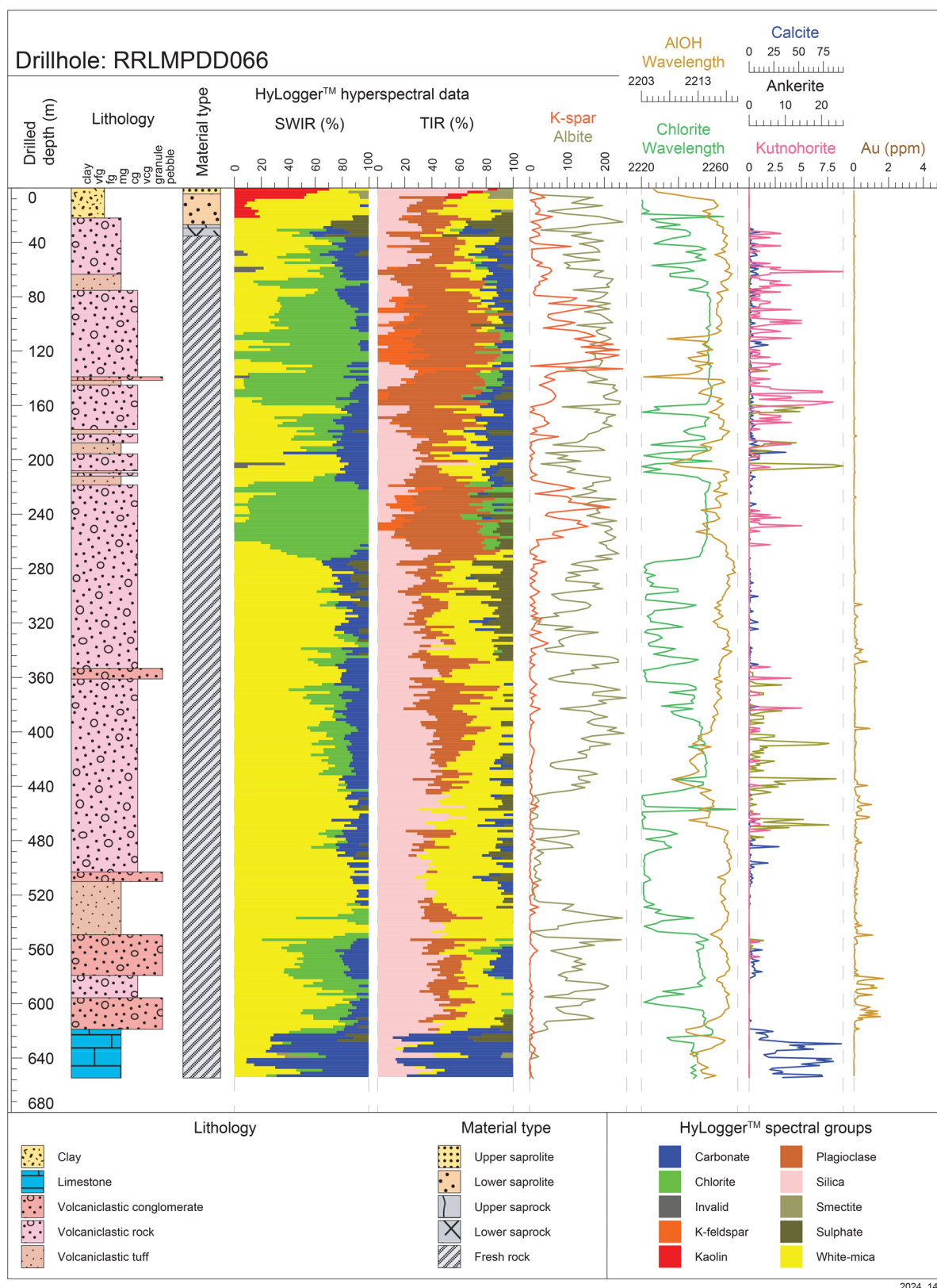
**Figure 6.** Lithological and hyperspectral down hole plot for the southern cross-section (drillhole RRLMPDD066). This figure is compiled from user TSA TIR and SWIR output plots combined with lithological logs, with carbonate classified in IoGas using TIR according to Green and Schodlok (2016). The plots were generated using the well log and borehole plotting software strater (https://www.groundwatersoftware.com/strater.htm). Also shown are the mineral abundance data for selected feldspar (albite, K-feldspar), carbonate (calcite, ankerite, kutnohorite) and shifts in wavelength features for white mica (Al–OH feature) and chlorite.
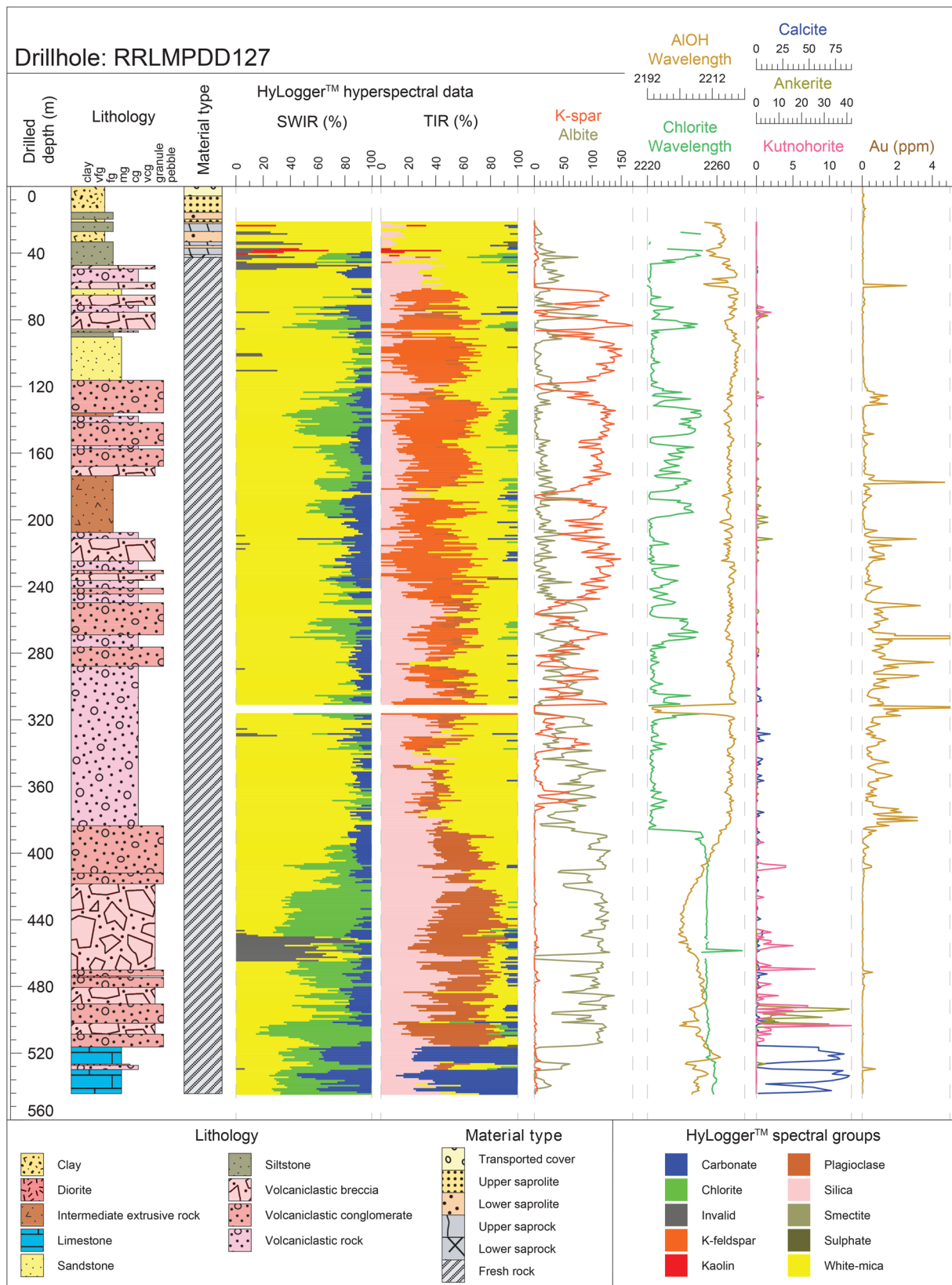
**Figure 7.** Lithological and hyperspectral down hole plots for the central cross-section (drillholes (a) RRLMPDD0127 and (b) RRLMPDD0214). This figure is compiled from user TSA TIR and SWIR output plots combined with lithological logs, with carbonate classified in ioGas using TIR according to Green and Schodlok (2016). The plots were generated using the well log and borehole plotting software strater (https://www.groundwatersoftware.com/strater.htm). Also shown are the mineral abundance data for selected feldspar (albite, K-feldspar), carbonate (calcite, ankerite, kutnohorite) and shifts in wavelength features for white mica (Al–OH feature) and chlorite.
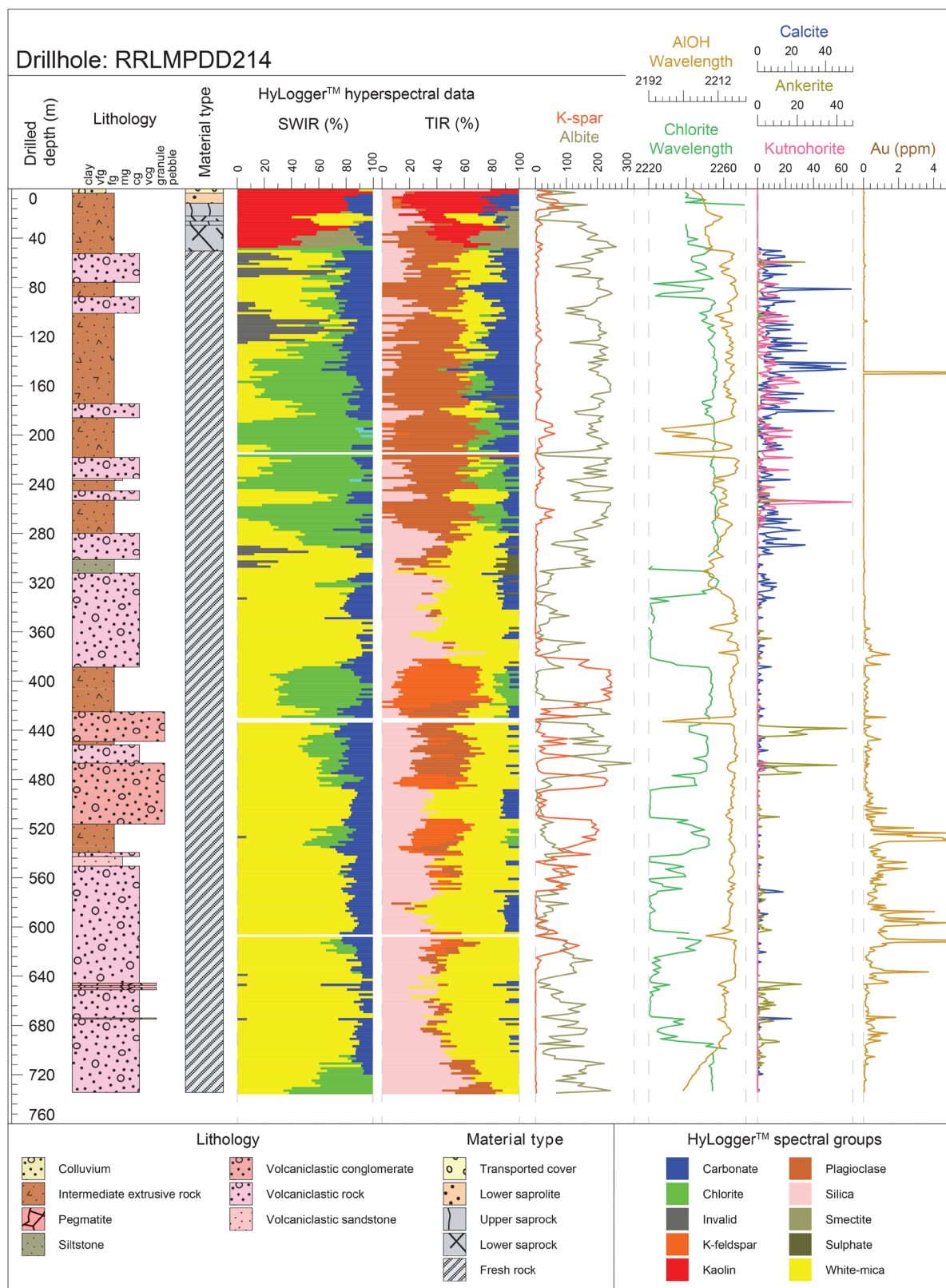
**Figure 7.** Continued.
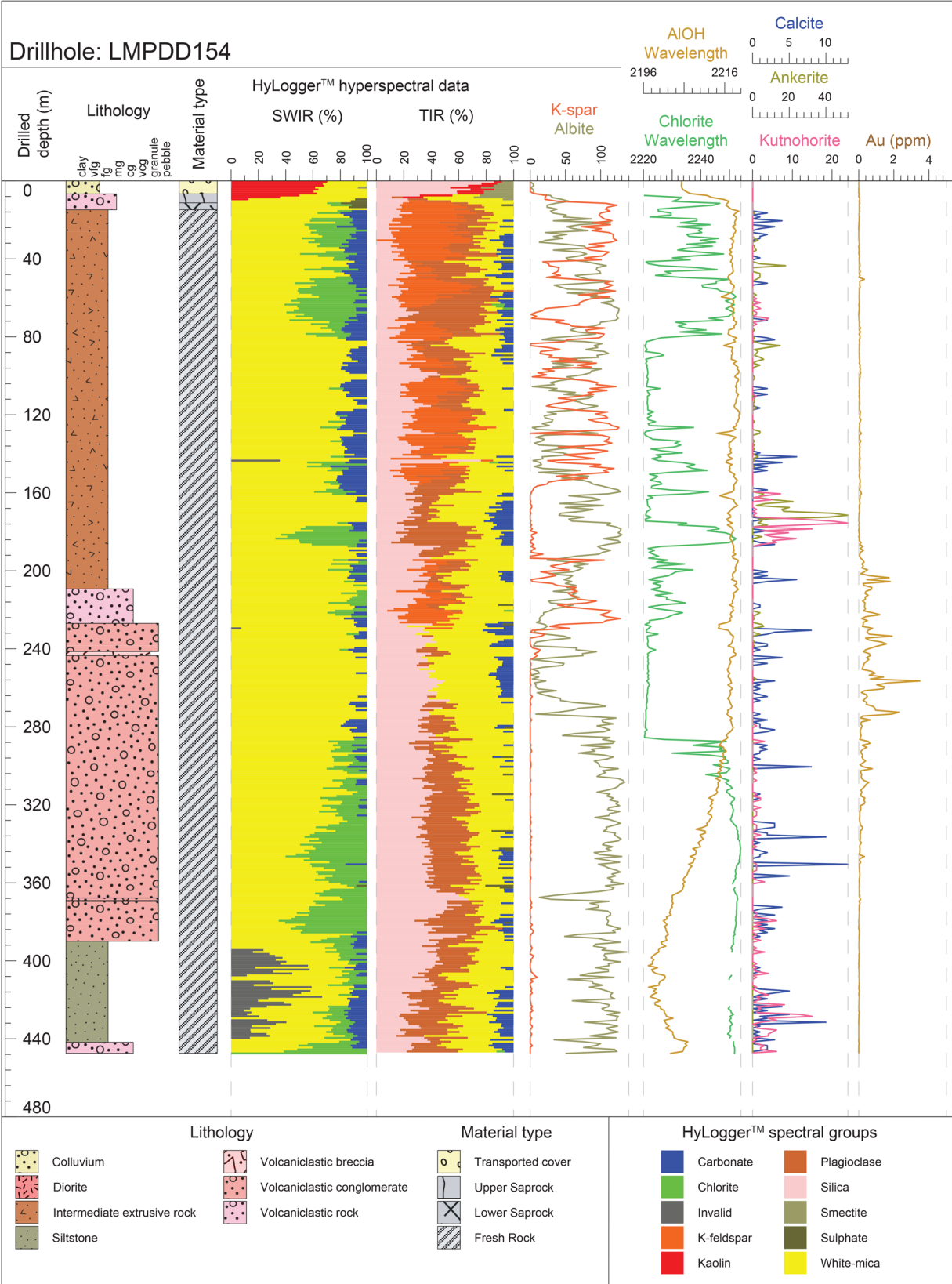
**Figure 8.** Lithological and hyperspectral down hole plots for the central cross-section (drillholes (a) RRLMPDD0154 and (b) RRLMPDD0205). This figure is compiled from user TSA TIR and SWIR output plots combined with lithological logs, with carbonate classified in IoGas using TIR according to Green and Schodlok (2016). The plots were generated using the well log and borehole plotting software strater (https://www.groundwatersoftware.com/strater.htm). Also shown are the mineral abundance data for selected feldspar (albite, K-feldspar), carbonate (calcite, ankerite, kutnohorite) and shifts in wavelength features for white mica (Al–OH feature) and chlorite.
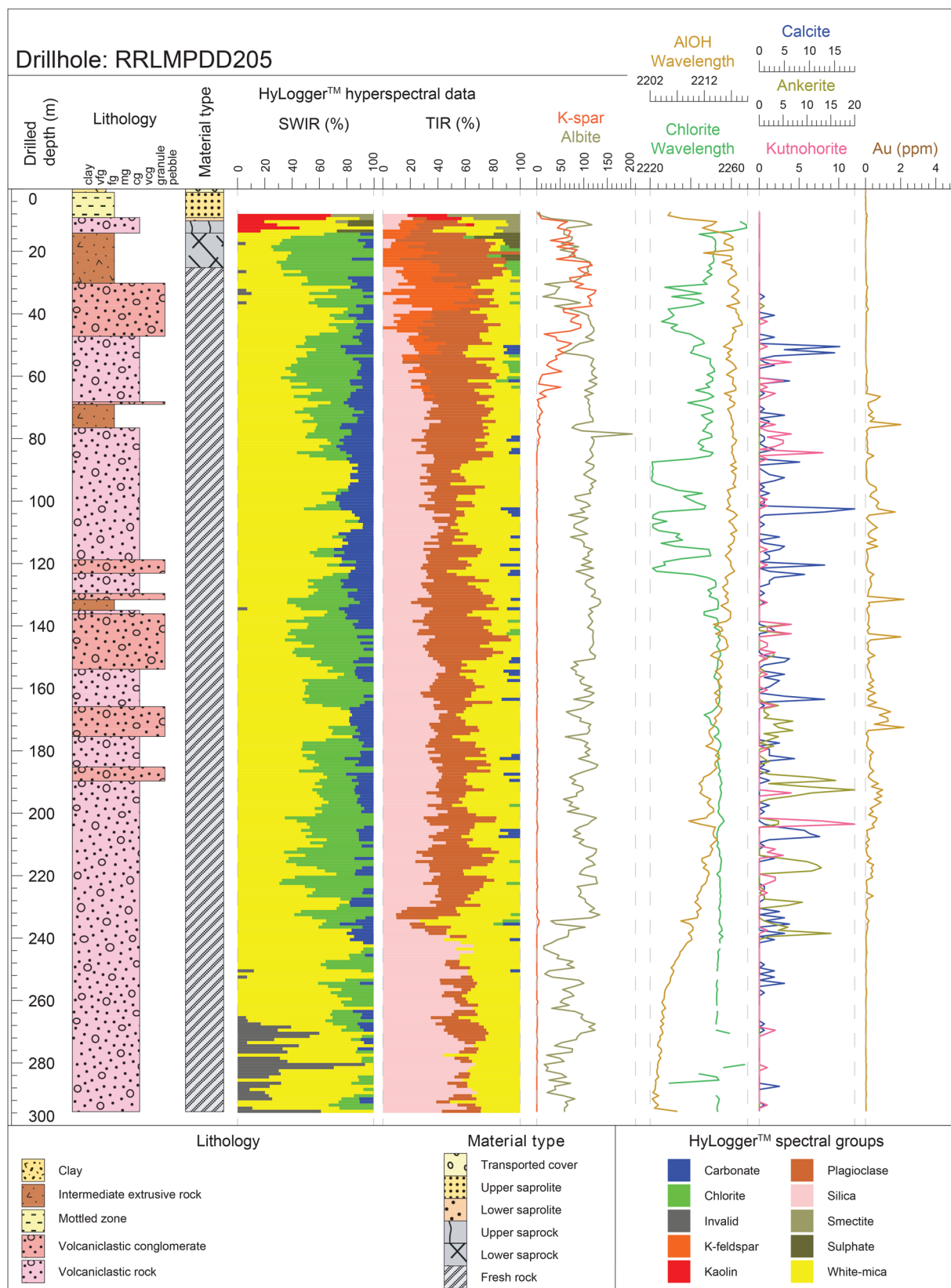
**Figure 8.** Continued.

Mg-rich compositions (wavelength 2248–2256 nm), while white mica is predominantly phengitic (Al–OH wavelength 2208–2218 nm). Carbonate in the hanging wall is dominated by calcite and kutnohorite, with a calcite dominant zone directly above the mineralised interval.

The mineralised interval is lithologically diverse, but the lithological-based mineralogical variation is less clear than for the hanging wall sequence. Alteration response of the mineralised interval includes abundant white mica, chlorite, K-feldspar, minor carbonate and very minor plagioclase (albite). Quartz abundance is variable and typically displays an inverse relationship with K-feldspar abundance. Chlorite is a mixture of Fe–Mg- and Mg-rich compositions in both RRLMPDD0127 and RRLMPDD0214 (Figure 7a, b), with chlorite wavelength varying between 2220 and 2250 nm. White mica is phengitic with a narrow Al–OH absorption feature ~2218 nm. Carbonate is not abundant in the mineralised interval aside for ankerite, particularly in hole RRLMPDD0214.

The footwall to mineralisation in the central zone includes both the lower, coarse volcaniclastics and an underlying calcareous package. The footwall alteration assemblage is best represented in hole RRLMPDD0127 and includes coarse-grained volcaniclastic sequences that comprise white mica, chlorite, carbonate and variable, but commonly roughly equal proportions of quartz and plagioclase (albite). Chlorite is mixed Fe–Mg and displays a rapid compositional shift to longer wavelengths (~2256 nm) on entering the unmineralised lower coarse-grained volcaniclastics. Chlorite is Fe–Mg- and lesser Fe-chlorite within the lower calcareous sequence with a shift to slightly longer wavelengths (~2260 nm). White mica is muscovite in the upper parts of the lower, coarse volcaniclastics in the footwall, but there is a gradual shortening of the Al–OH wavelength (to ~2202 nm) between 390 and 440 m. The white mica composition is variable beneath this zone with mixed phengitic/muscovitic white mica, and the Al–OH feature wavelength fluctuates between 2202 and 2216 nm. Carbonate in the lower coarse-grained volcaniclastic package is dominated by kutnohorite with lesser calcite. There is a narrow ankerite spike at the base of the volcaniclastic package close to the contact with the underlying calcite dominant calcareous sequences.

*Northern section.* Mineralisation in drillholes RRLMPDD154 and RRLMPDD205 (Figure 8a, b) is hosted within the upper, coarse volcaniclastic package.

In RRLMPDD205, the hanging wall to mineralisation comprises an upper sequence of interbedded intermediate extrusive rocks (andesitic lava/volcaniclastic package) and volcaniclastic rocks of the upper, coarse volcaniclastic package. By contrast, in RRLMPDD154, lithology is unsubdivided, and the dominant lithology is very broadly logged as intermediate extrusive. Hanging wall intervals of intermediate extrusive rocks and volcaniclastics in RRLMPDD154 and the top of RRLMPDD205 comprise an alteration assemblage of white mica, chlorite, K-feldspar, plagioclase (albite) and carbonate with only moderate quartz abundance. There is cyclic repartition in the relative abundance of these minerals, likely reflecting unrecognised lithological variation. The feldspar-enriched intervals typically have lower modal quartz and can be enriched in carbonate ± chlorite. These intervals are consistent with the upper, coarse volcaniclastic

package logged elsewhere in the deposit. The feldspar-enriched zones are separated by narrow zones of white mica and quartz that generally lack carbonate and K-feldspar but have variable plagioclase. Where present, chlorite is predominantly mixed Fe–Mg with a moderate compositional range (wavelength 2235–2251 nm), while white mica is phengitic (Al–OH wavelength ~2218 nm). Carbonate is not abundant in the hanging wall and is a mix of ankerite, kutnohorite and calcite. Ankerite and kutnohorite are dominant towards the base of the hanging wall sequence in RRLMPDD154.

The mineralised interval in RRLMPDD205 (65–235 m) is logged as an interbedded sequence of medium- to coarse-grained volcaniclastic rocks, with the higher-grade Au zone commonly corresponding with coarser-grained intervals. The alteration assemblage here includes white mica, chlorite, plagioclase (albite) and carbonate with moderate quartz abundance. In the upper parts of the mineralised interval, there is a domain between 85 and 120 m that is chlorite-poor and relatively depleted in plagioclase. A similar domain also occurs in the mineralised interval of drillhole RRLMPDD154 (234 to ~280 m). Above this zone in RRLMPDD205, chlorite is mostly mixed Fe–Mg with minor Mg and moderate compositional range (wavelength 2240–2252 nm). Below this, the chlorite is also mixed Fe–Mg- with minor Fe-chlorite and has a consistent chlorite wavelength ~2254 nm. For drillhole RRLMPDD154, the chlorite-poor domain is flanked by mixed Fe–Mg- and Mg-chlorite (~2230–2248 nm), with a wavelength progressively widening to 2254 nm at the base of the mineralised interval. White mica is phengite (Al–OH wavelength 2217 nm) with a small shift to shorter wavelengths (Al–OH wavelength 2214 nm) below the chlorite-poor domain. Towards the base of the mineralised interval in RRLMPDD154 and at the base of the mineralisation in RRLMPDD205, the white mica wavelength shortens towards muscovitic compositions more typical of the footwall alteration zone. Carbonate is mostly calcite with lesser kutnohorite, while ankerite is abundant in the lower half of the mineralised interval in hole RRLMPDD205.

The lower, coarse volcaniclastic package is the footwall to mineralisation in the northern part of the orebody where it is underlain by a package that includes siltstone interbeds. Logged intervals of volcaniclastic comprise white mica, chlorite, plagioclase (albite) with minor carbonate and moderate quartz abundance. The siltstone-rich interval intersected at the base of both drillholes has a strong to moderate aspectral response with white mica, minor chlorite and variable carbonate. The footwall in drillhole RRLMPDD154 is characterised by Fe–Mg- and Mg-chlorite with a lengthening of wavelength 2248–2250 nm, while the wavelength shift is less clear in RRLMPDD205. White mica is muscovite in the footwall, with a shift to shorter Al–OH wavelengths (RRLMPDD205 ~2204 nm and RLMPDD154 ~2198 nm) from the base of the mineralised interval. Carbonate in the footwall comprises variable proportions of kutnohorite and calcite.

### 3D modelling of hyperspectral alteration data

Numerical 3D modelling was conducted on alteration mineral abundance data integrated with gold assay and lithological data using Seequent's Leapfrog Geo software. White mica, feldspar,

quartz, chlorite and carbonate were modelled separately with several discrete and broad trends observed.

Stage$_1$ alteration is characterised by variable feldspar species, including a K-feldspar-rich inner zone associated with gold, flanked by albite (Figure 9). The modelled albite appears flattened at the surface, carrot-shaped and more associated with the footwall side of the higher-grade gold. This apparent trend may also reflect the data density with a decrease in sample points with depth and into the hanging wall. The distal nature of the modelled albite to inner K-feldspar core is still observed, while the microcline model appears to have a positive correlation with gold mineralisation.

Modelling of phengitic and muscovitic white micas, interpreted as stage$_2$ alteration, shows a distinct association between gold and the change in white mica species (Figure 10). Gold displays a positive association with phengitic white mica, while there is a distinct lack of gold where muscovite is abundant. Muscovite is concentrated in the footwall to mineralisation. This switch from phengite to muscovite has previously been related to a footwall fault. Closer to the surface (900 mRL plan) phengite appears to dominate, most likely reflecting the weathering profile.

The chlorite abundance model (Figure 11) shows that the Mg-rich end-member is associated with the high-grade gold core. Fe-rich chlorite is associated with the periphery to this core and shows a negative association with gold. Modelling of

carbonate abundance (Figure 12) shows positive associations between ankerite and kutnohorite to gold. Calcite and kutnohorite are the main carbonate species in the propylitic alteration zone peripheral to the mineralisation (Figure 12).

### New geochronology for host rocks and mineralisation

Twelve U–Pb SHRIMP dating analyses were carried out on eight zircon grains recovered from a potassic-altered intermediate volcaniclastic rock located within the main gold interval. Four analyses on four of these grains reflect Paleoproterozoic inheritance. The remaining eight analyses were carried out on the other four zircon grains. After excluding one analysis that sampled a domain affected by loss of radiogenic Pb (date of *ca* 368 Ma, after the crystal grain had already yielded two mid-Silurian spot ages), the remaining analyses returned ages that ranged from 434 to 418 Ma and define a statistically coherent mean at 427 ± 6 Ma (95% confidence; MSWD = 1.64, n = 7).

LA-ICP-MS U–Pb dating of titanite from a volcaniclastic (McPhil01, drillhole RRLMPD066, 333.1–333.4 m) was conducted in three sessions and defined discordia regressions with lower-intercept ages of, 391 ± 15 Ma with a MSWD of 0.66 (n = 40, $^{207}$Pb/$^{206}$Pb = 0.761 ± 0.043), 391 ± 11 Ma with a MSWD of 0.84 (n = 33, $^{207}$Pb/$^{206}$Pb = 0.833 ± 0.025) and 397 ± 9.5 Ma with a MSWD of 1.4 (n = 42, $^{207}$Pb/$^{206}$Pb = 0.842 ± 0.034).
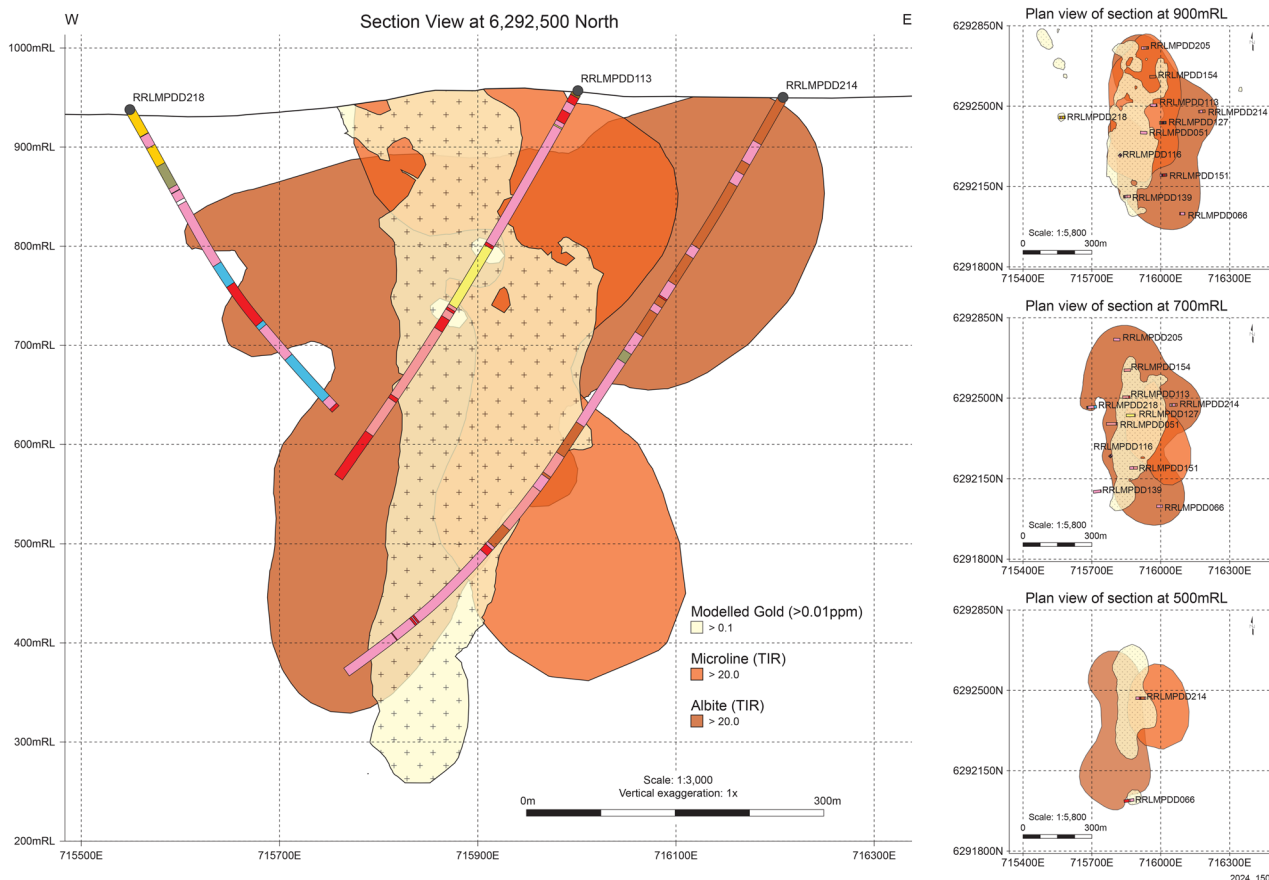


**Figure 9.** Sectional and plan views of the results from modelling feldspar alteration (albite and K-feldspar) abundance identified in the downhole TIR data.
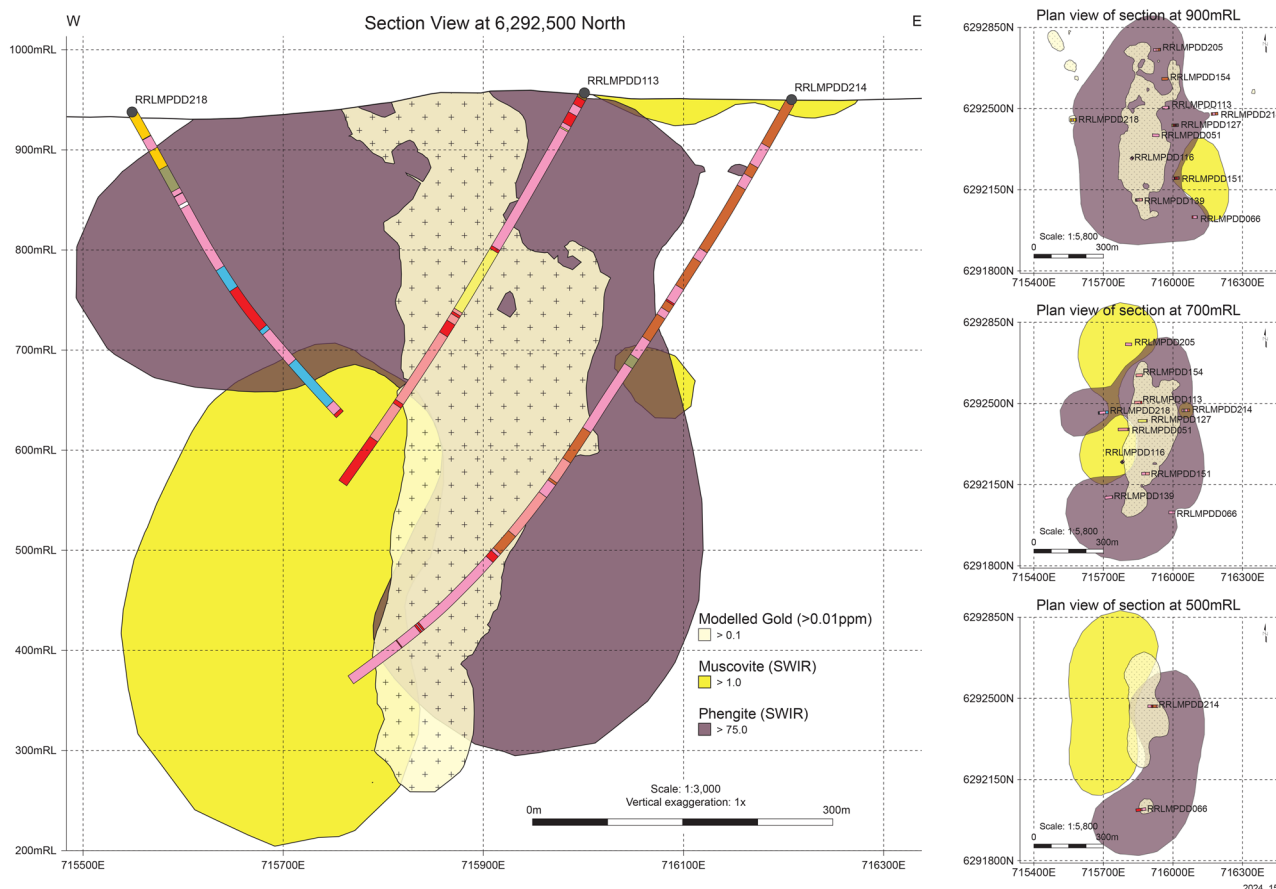
**Figure 10.** Sectional and plan views of the results from modelling the white mica alteration (phengite and muscovite) abundance identified in the downhole SWIR data.

A second titanite sample (McPhil02, drillhole RRLMPDD214, 290.5–290.7 m), which was intergrown with cubic pyrite$_2$ within a quartz vein located in the hanging wall to mineralisation, was also analysed over three sessions, but the titanite are rare and display little variation in U content. Titanite from the three sessions display variability in their discordia regression lower-intercept ages and high uncertainties, including $399 \pm 25$ Ma with an MSWD of 1.2 (n = 38, $^{207}$Pb/$^{206}$Pb = $0.872 \pm 0.032$), $377 \pm 18$ Ma with an MSWD of 0.95 (n = 32, $^{207}$Pb/$^{206}$Pb = $0.848 \pm 0.016$) and $389 \pm 31$ Ma with an MSWD of 1.0 (n = 36, $^{207}$Pb/$^{206}$Pb = $0.718 \pm 0.028$).

The high-precision Pb data from Huston et al. (2016) and this study provide an independent measure of the common $^{207}$Pb/$^{206}$Pb at the time of mineralisation at McPhillamys with $^{207}$Pb/$^{206}$Pb ratios for three galena and a single whole-rock sample ranging between 0.852 and $0.855 \pm 0.003$ (see supplemental data). These high-precision Pb ratios are consistent with the discordia regression $^{207}$Pb/$^{206}$Pb intercepts for titanite analysed from the two McPhillamys samples, except for the first session for Mcphil01 and the last session for Mcphil02. The combined data suggest the age of titanite intergrown with cubic pyrite$_2$ at McPhillamys is ca 390 Ma.

Step-heating of muscovite intergrown with cubic pyrite$_{2-3}$ in a foliated pyrite, muscovite, quartz altered volcaniclastic (sample McPhil03, drillhole MPRCD015, 509.35–510.45 m) for $^{40}$Ar/$^{39}$Ar dating gave a flat age spectrum with a well-defined plateau age of $351.1 \pm 4.0$ Ma with an MSWD of 1.6 (including J-error of 0.51%) for four steps within the plateau (plateau includes 62.8% of the $^{30}$Ar).

Lead model age estimates were calculated for four high-precision Pb-isotope analyses for galena-rich samples from Huston et al. (2016). Three of the analyses gave Pb-model ages that lie within error at ca 423 Ma (range 425–420 Ma), while the fourth gave a younger Pb-model age of 395 Ma.

### Sulfur isotopes

Twenty-nine sulfur-isotope analyses were carried out on disseminated and vein-hosted sulfides from within the Au-bearing alteration zone at McPhillamys. δ$^{34}$S values range between −15.0 and 22.6‰ VCDT with most analyses forming a tight cluster between −0.9 and 2.7‰ VCDT (mean δ$^{34}$S 1.4‰ VCDT—23 analyses) (Table 1). Excluding outliers, δ$^{34}$S values for pyrite average 1.5‰ VCDT (range 0.7–2.6‰ VCDT, 12 analyses), those for chalcopyrite average 0.9‰ VCDT (range 0.1–1.6‰ VCDT, 6 analyses), and those for sphalerite average 1.8‰ VCDT (range 1.0–2.7‰ VCDT, 4 analyses); galena has values of −0.9, 2.0 and 5.0‰ VCDT.
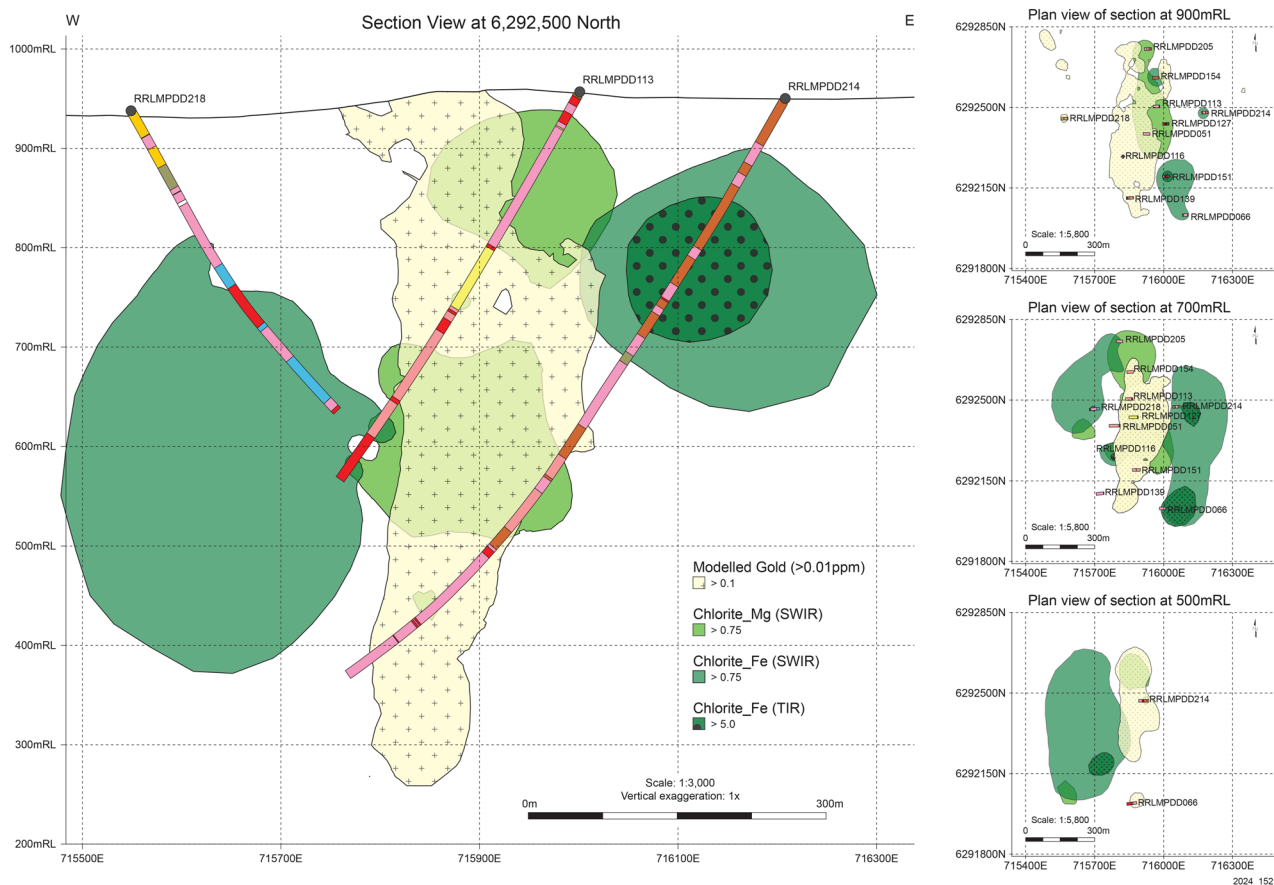
**Figure 11.** Sectional and plan views of the results from modelling the chlorite alteration (Mg-rich and Fe-rich) abundance identified in the downhole SWIR data.

## Discussion

### *Alteration/mineralisation paragenesis*

Mineralisation and alteration are multiphase within the McPhillamys gold system, and although geochronology was not able to determine the absolute timing of mineralisation and alteration, a robust paragenesis can be constructed based on new and previously known characteristics including:

1. Pyrite from within a mineralised potassic-altered zone has been shown to be multiphase by Fitzherbert *et al.* (2024) and involves probable low temperature (200–300 °C) pyritohedron pyrite$_1$ cores that are rich in inclusions of K-feldspar, albite, Fe-dolomite and host lattice bound gold. These cores are surrounded by higher temperature (>300 °C) silicate inclusion-free euhedral cubic pyrite$_2$ rims that are commonly in contact with biotite-rich strain fringes and are barren with respect to Au. Both core and rim have been modified through subsequent diffusion to gold and inclusion-free pyrite$_3$ rims that are developed on the high strain faces of the grains at the contact with the foliation.

2. U–Pb zircon dating constrains the age of the host volcaniclastic sequences to 427 ± 6 Ma. Titanite intergrown with euhedral cubic pyrite$_2$ rims returned a U–Pb age of *ca* 390 Ma consistent with rim growth during Tabberabberan deformation. Phengite intergrown with pyrite$_{2-3}$ rims preserve a younger Ar–Ar age of *ca* 350 Ma, consistent with a second Kanimblan pulse of deformation. The pyrite$_1$ cores have not been directly dated.

3. Lead model ages calculated using high-precision data for galena-rich samples from Huston *et al.* (2016) gave ages of *ca* 423 Ma possibly suggesting that mineralisation was latest Silurian in age, with a single Devonian model age that may be consistent with orebody deformation during Tabberabberan deformation.

4. Stage$_1$ alteration has a strongly potassic core, with K-feldspar (microcline), ankerite and pyrite locally preserved in areas of low strain; textual evidence is consistent with the presence of adularia in the potassic core prior to deformation and development of microcline. The potassic alteration is overprinted by stage$_2$ phengitic white mica with pyrite.

5. Biotite likely crystallised during deformation and schistose phengitic white mica may reflect recrystallised illite.

Based on these characteristics we interpret a paragenesis that evolved from early development of stage$_1$ adularia (now microcline), ankerite and minor chlorite and inclusion-rich Au-bearing dodecahedral pyrite, overprinted by stage$_2$ phengite (potentially
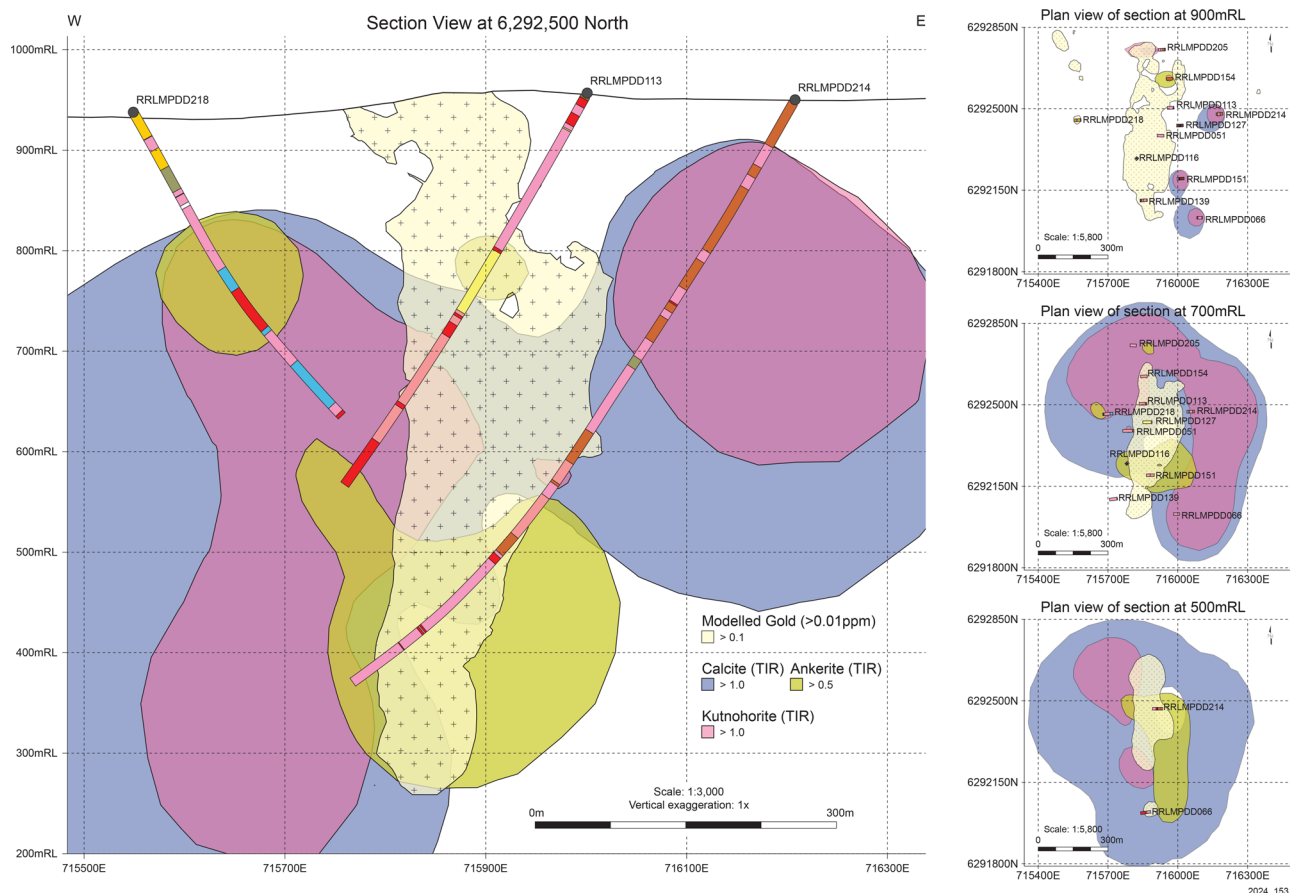
**Figure 12.** Sectional and plan views of the results from modelling the carbonate alteration abundance (calcite, kutnohorite, ankerite) identified in the downhole TIR data.

ex-illite). At the same time the surrounding propylitic shell developed albite, chlorite, Mn- and Ca-carbonate along with a locally pervasive phengite (muscovite in the footwall) and generally Au-barren pyrite. Titanite geochronology records deformation during the *ca* 390 Ma Tabberabberan Orogeny, timing the crystallisation of euhedral pyrite$_2$ rims (>300 °C) and crystallisation of biotite and phengite. Early-formed adularia was likely converted to microcline during this event. Tabberabberan deformation was followed by the *ca* 350 Ma Kanimblan deformation, resulting in chemical modification of pyrite$_{1-2}$ owing to strain induced element diffusion and further recrystallisation of the greater orebody to form a 3$^{rd}$ and final generation of pyrite.

### *The relationship between deposit-scale stratigraphy, alteration and mineralisation*

The stratigraphy that hosts the McPhillamys orebody is correlated through all 11 drillholes (summarised through seven drillholes in Figure 5) and comprises a lower calcareous sequence overlain by two (lower and upper) distinctive packages of coarse dacitic to andesitic volcaniclastics that are separated by a finer-grained, feldspar-poor sequence, which has been variably logged as sandstone and finer-grained volcaniclastics. The upper most sequence exposed in the drill core comprises interbedded andesitic volcanic and lesser volcaniclastic rocks. Gold

mineralisation is localised to the upper coarse-grained volcaniclastics and underlying finer-grained feldspar-poor volcaniclastics/sandstones and extends into the lower volcaniclastic package at the southern end of the orebody (*e.g.* drillhole RRLMPDD066).

The two stages of alteration at McPhillamys display slightly different spatial relationship with mineralisation and stratigraphy (Figure 14); it is important to note that the altered zone has been extensively recrystallised, but we suggest the mineralogy still preserves the chemical zonation and in places mineralogy that developed prior to deformation. Stage$_1$ alteration involves the development of a flattened conical-shaped potassic zone surrounded by an outer propylitic shell. The potassic zone is characterised by early-formed adularia (now microcline), calcite–kutnohorite, locally abundant ankerite (mostly in the lower coarse-grained volcaniclastic sequence and at the base of the upper coarse-grained volcaniclastic sequence), and chlorite-replaced biotite (undetected by HyLogger). In the centre of the orebody this zone is developed within the upper, coarse volcaniclastic package and broadly coincides with Au mineralisation. In the south, the potassic alteration becomes weaker and is developed at higher stratigraphic levels within the andesitic volcanic/volcaniclastic package but no longer coincides with mineralisation. To the north, the potassic alteration also moves progressively higher in the stratigraphy with drillhole
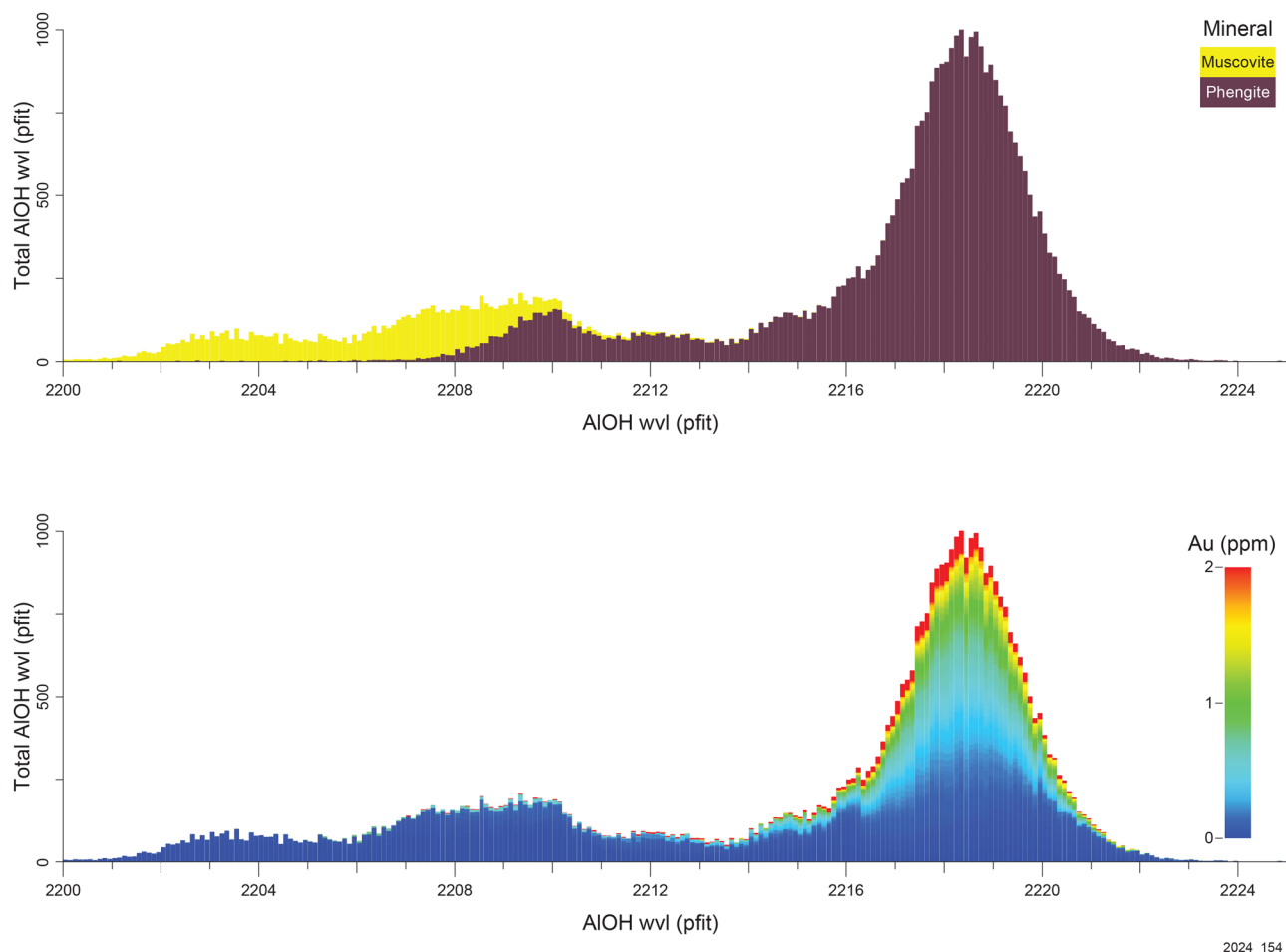
**Figure 13.** Plots of white mica Al–OH wavelength for core from drillhole RRLMPDD127. Upper image illustrates the distribution of phengite *vs* muscovite. The lower image illustrates the relationship between Al–OH wavelength and Au abundance. Similar plots for all drillholes used in this study can be found in the supplemental data.

RRLMPDD205 intersecting K-feldspar-rich alteration at the base of the andesitic lava/volcaniclastic package and again it is no longer coincident with mineralisation. Stage$_1$ propylitic-style alteration comprises chlorite, albite, kutnohorite and calcite. There is commonly an ankerite dominant zone developed within the lower coarse-grained volcaniclastic package directly above the contact with the lower calcareous package. Mineralisation was not observed within propylitic alteration within the upper most andesitic volcanic/volcaniclastic package, but Au mineralisation has developed in the propylitic-altered upper and lower coarse volcaniclastic packages in the southern part of the orebody (*e.g.* drillhole RRLMPDD066) and within propylitic-altered lithologies of the upper, coarse volcaniclastic package in the northern part of the orebody (*e.g.* RRLMPDD205). The lower calcareous package is never mineralised and where sampled displays the secondary mineralogy (chlorite and white mica) consistent with the overlying lower coarse-grained volcaniclastic package, but carbonate here is calcite.

Stage$_2$ alteration is dominated by white mica and pyrite defining a schistose foliation. White mica composition displays a strong correlation with Au mineralisation (Figure 13 for drillhole RRLMPDD127—plots for all drill holes are presented in the supplemental data). In the propylitic-altered hanging wall sequence and the mineralised upper coarse-grained volcaniclastic sequence white mica is mostly phengitic. For the hanging wall sequence the Al–OH wavelength is variable (2208–2218 nm) while within the mineralised upper coarse-grained volcaniclastic sequence it typically displays a restricted Al–OH wavelength between 2216 and 2218 nm, although this may slowly shift to shorter wavelength towards the base of the mineralisation. This restricted Al–OH wavelength is maintained throughout the mineralised interval irrespective of the mineralogy developed during stage$_1$ alteration (*i.e.* in both potassic and propylitic zones). However, there is always a significant shift in the white mica to shorter Al–OH wavelengths (~2204 nm) at the top of the footwall sequences (either in the lower coarse-grained volcaniclastics or the underlying calcareous package) where it shifts to muscovitic compositions. The change in white mica composition from the mineralised interval mostly occurs at the boundary between the upper and lower coarse volcaniclastic packages and may extend into the lower coarse volcanic package. The Sherlock fault has also proposed to be located at this boundary.
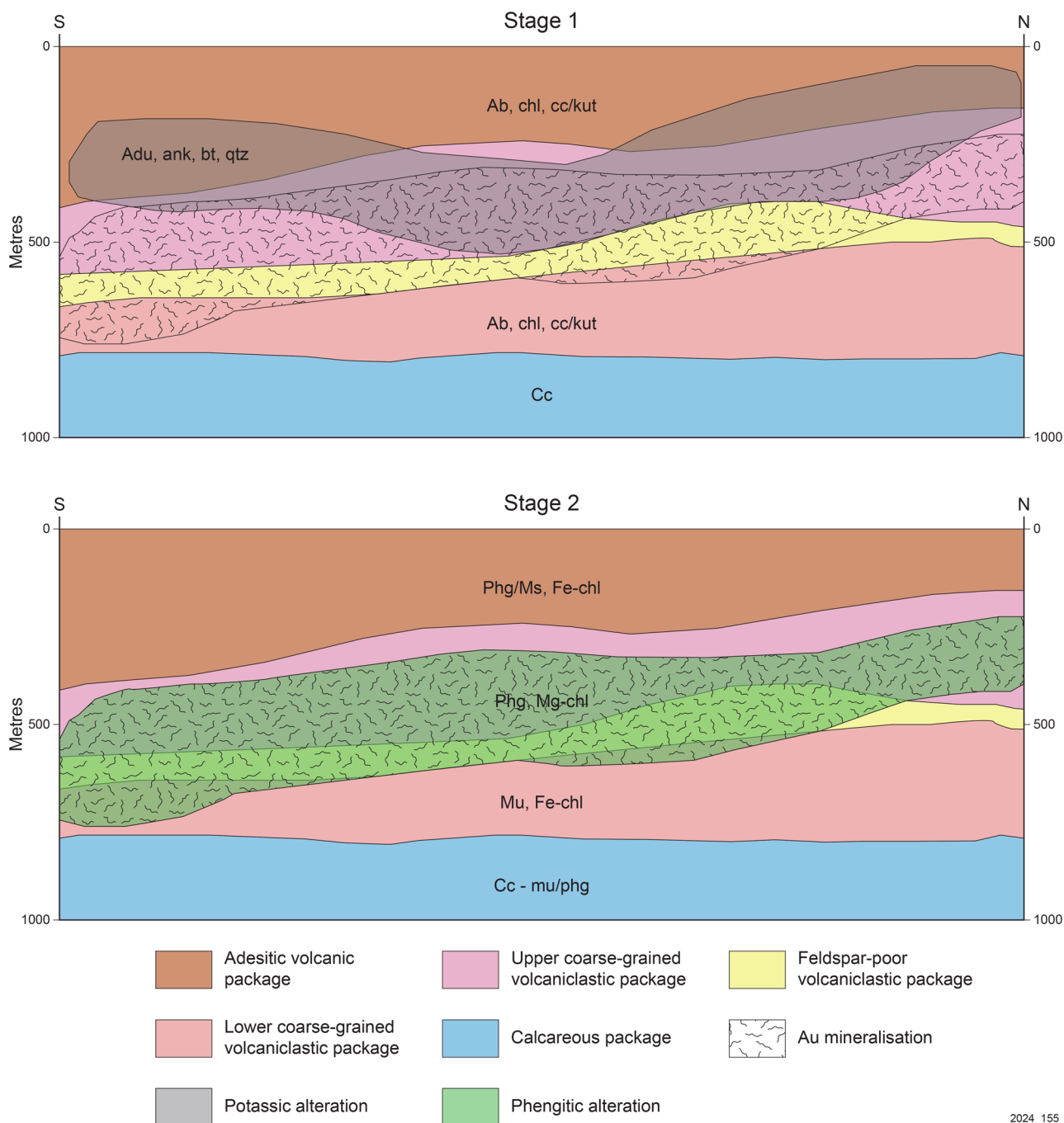
**Figure 14.** Simple diagrammatic two stage model for the pre-deformation distribution and mineralogy of alteration with respect to mineralisation and lithology. Mineral abbreviations are ab, albite; adu, adularia; ank, ankerite; cc, calcite; chl, chlorite; kut, kutnohorite; phg, phengite; mu, muscovite.

### Ore genesis

Deformation of the McPhillamys orebody partially masks the character of early alteration and mineralisation and it is difficult to reconstruct the primary lithological and alteration mineralogy of the mineralised zone through conventional core logging. Based on our petrographic and hyperspectral work the McPhillamys mineralised body is, on a gross-scale, associated with an extensive (>700 m length), lithologically controlled flattened conical alteration zone of K-feldspar (microcline), phengitic white mica, silica and Fe–Mn carbonate (ankerite/kutnohorite), with lesser Fe-chlorite associated with stringer vein-hosted and disseminated Au-enriched pyrite (Figure 14). This zone is interpreted to reflect extensive initial pyrite$_1$–gold mineralisation associated with potential pre-deformation adularia–sericite (illite) –pyrite–silica–carbonate alteration. This potassic zone is flanked by a propylitic-style alteration shell involving albite, Mg-chlorite, mostly muscovitic white mica calcite/kutnohorite, pyrite, with or without epidote. The broad-scale and lithological control of the pyritic Au±Cu mineralisation

and association with K-feldspar (microcline after adularia)–sericite (illite)–pyrite–silica and lesser carbonate alteration may be consistent with two possible models of formation, that include (1) a disseminated, low-sulfidation epithermal system that has exploited a permeable volcaniclastic host sequence, and (2) epizonal to mesozonal orogenic gold mineralisation formed through prograde devolatilisation of the underlying basement.

Permeable host-rock control is reportedly not common for low-sulfidation epithermal systems (*e.g.* Corbett 2012), although the widely dispersed low Au-grades and size of the alteration/mineralisation at McPhillamys is entirely consistent with the lithologically controlled low-sulfidation epithermal model of Hedenquist *et al.* (2000) and a number of other significant systems including the Hauraki goldfield (NZ, Simpson & Christie, 2019), Round Mountain (USA, Henry *et al.*, 1997; Rhys *et al.*, 2020), La Coipa (Chile, Oviedo, *et al.*, 1991) and El Peñón (Chile, Morales-Leal, *et al.*, 2022), with overlying andesitic lavas likely to act as a part seal to the mineralising fluid. The inner zone of potassic alteration at McPhillamys, with potassic, ex-adularia and/or illite, carbonate and pyrite, is characteristic within low- and intermediate-sulfidation deposits formed from reduced, near-neutral pH to alkaline fluids (Hedenquist *et al.*, 2000; White & Hedenquist, 1995). By contrast, the magnetite (hematite)-bearing propylitic alteration in the footwall (lower coarse-grained volcaniclastic sequence) suggest slightly more alkaline and potentially oxidised conditions developed external to the central potassic zone. The early textural relationships at McPhillamys are poorly preserved owing to structural overprinting. However, there is textural evidence for boiling and a range of textures in preserved vein fragments (*e.g.* crustiform and colloform banding, chalcedonic quartz and bladed calcite±epidote veins) that are common to epithermal systems (*e.g.* Dong *et al.*, 1995). Adularia deposition, through gas loss and pH increase, is also considered evidence for boiling and good permeability in epithermal systems (*e.g.* Çam *et al.*, 2018; Henley, 1985; Simmons *et al.*, 2000). At McPhillamys, the K-feldspar (microcline after early adularia) replacement is pervasive and commonly texturally destructive. In addition, the bladed carbonate in calcite±epidote veins locally display evidence of silica replacement, another texture widely linked to boiling and consistent with gas loss and cooling in an epithermal environment (*e.g.* Simmons & Browne, 2000).

A model involving devolatilisation of the host rock (or more likely underlying mafic to intermediate basement) and gold deposition during Tabberabberan deformation remains viable and is not disproved by the geochronology presented in this study. In this model the proposed Sherlock fault is an important feature as a potential fluid conduit located at the boundary between the unmineralised footwall and mineralisation, with mineralising fluids potentially taking advantage of the reactive overlying sequences. Although the absolute timing of sieved (inclusion-rich) pyrite$_1$ cores could not be determined, we suggest formation at temperatures ~200–300 °C, along with the presence of internal K-feldspar inclusions described by Fitzherbert *et al.* (2024) is most consistent with initial pyrite$_1$–Au mineralisation occurring synchronous with and spatially associated with the initial potassic assemblage and to a lesser degree with propylitic assemblage. Thus, in an orogenic model

potassic alteration would be considered to have developed early in the mineralising event along with Au-bearing pyrite$_1$, while euhedral, Au-barren pyrite$_2$ rims developed during increased temperature and further deformation. For this model current U–Pb dating suggests a minimum age for mineralisation during Tabberabberan deformation at *ca* 390 Ma. δ$^{34}$S values of −0.9 and 2.7‰ VCDT for sulfide minerals may also be consistent with sulfur being sourced from the underlying intermediate to mafic magmatic basement rocks.

Although a Tabberabberan orogenic model is not disproved, potassic alteration haloes to the broad extent of that preserved at McPhillamys are not commonly described for greenschist facies (epizonal to lower mesozonal) orogenic gold deposits (Goldfarb & Groves, 2015), which are typically characterised by quartz–carbonate–white mica–chlorite–pyrite (±albite) alteration related to carbonic fluids (see Goldfarb *et al.*, 2005; Goldfarb & Groves, 2015; Li *et al.*, 2022; McCuaig & Kerrich, 1998). K-feldspar (in abundance) is typically described for higher temperature/deeper-formed (hypozonal) deposits, commonly along with abundant biotite (Li *et al.*, 2022). Goldfarb *et al.* (2005) also documents a general dearth of vertical and along strike zonation associated with most epizonal orogenic Au systems. Nevertheless, less extensive K-feldspar-rich alteration haloes (up to 30 m from the causative shear zone) as well as K-feldspar early in the mineralising event (*e.g.* Zhao *et al.*, 2023) have been described for some epizonal orogenic deposits.

Based on the alteration style, alteration footprint, paragenesis and available geochronology for mineralisation at McPhillamys we favour a lithologically controlled low-sulfidation epithermal model that potentially shares some characteristics with Au-rich (subsea-floor) VMS deposits (*e.g.* Bousquet, Dube *et al.*, 2014; and other Au-rich VMS deposits of the Abitibi). Interestingly, the very tight cluster of sulfur-isotope data between −0.9 and 2.7‰ VCDT for McPhillamys overlap with the range δ$^{34}$S values for normal igneous sulfur (0±2‰ VCDT; Ohmoto & Rye, 1979) and suggest that most of the sulfur included in the system was sourced from a reservoir dominated by magmatic sulfur. The very minor trend towards $^{34}$S-enriched values suggests that some sulfur was also sourced from the host-rock sequence or from a reduced late Silurian–earliest Devonian seawater sulfate source. However, the data are not consistent with significant late Silurian–Lower Devonian seawater being involved in ore formation as would be expected in a large volcanic-associated massive sulfide deposit such as Woodlawn (Ayres *et al.*, 1979; Glen *et al.*, 1995). A syngenetic or immediately post syngenetic timing (*ca* 425–423 Ma) for mineralisation is also consistent with Pb-isotope data (Pb-model age of *ca* 423 Ma; data from Huston *et al.*, 2016), while deformation ages for pyrite$_{2–3}$ rims are consistent with reworking of the deposit during the Tabberabberan Orogeny, with foliated white mica preserving evidence for subsequent deformation during the Kanimblan Orogeny.

## Conclusions

Petrographic analysis, hyperspectral scanning and geochronology have been successfully combined at McPhillamys to develop an alteration/mineralisation paragenesis and to map

the large-scale alteration footprint associated with mineralisation. Early stage$_1$ alteration involved a potassic-altered core, flanked by propylitic alteration zone, and is pervasively overprinted by a later stage pyrite + sericite alteration; the primary mineral assemblages have been modified by metamorphism and deformation. These two styles of alteration are spatially associated with mineralisation and likely occurred in close succession. The mineralisation and alteration have been shown to be broadly stratigraphically controlled (hosted in coarse volcaniclastic rocks) and there are distinctive compositional trends for white mica, chlorite, feldspar, carbonate and associated with mineralisation that can be mapped in 3D. Although our study does not categorically dismiss an orogenic Au model for McPhillamys, we contend that the alteration/mineralisation mineralogy, paragenesis (including geochronology) combined with the broad spatial distribution of alteration at McPhillamys is consistent with mineralisation representing a lithologically controlled late Silurian low-sulfidation epithermal or potentially shallow water Au-enriched VMS, that has been deformed and modified during the Tabberabberan and Kanimblan deformation events.

## Acknowledgements

## Disclosure statement

No potential conflict of interest was reported by the authors.

## ORCID

J. Fitzherbert http://orcid.org/0000-0003-2194-6949
P. Downes http://orcid.org/0000-0002-3979-1845
C. Folkes http://orcid.org/0000-0001-9239-3224
S. Bodorkos http://orcid.org/0000-0001-8605-0276
H. Huang http://orcid.org/0000-0002-0104-7201

## Data availability statement

The data supporting the findings of this study are available in the supplemental data of this paper or several Geological Survey of NSW data sharing platforms including MinView (https://minview.geoscience.nsw.gov.au/), DIGS (https://search.geoscience.nsw.gov.au/) and the NVCL (National Virtual Core Library https://portal.auscope.org.au/).

## References

Ayres, D. E., Burns, M. S., & Smith, J. W. (1979). Sulphur-isotope study of the massive sulphide orebody at Woodlawn, New South Wales. *Journal of the Geological Society of Australia*, *26*(3-4), 197–201. https://doi.org/10.1080/00167617908729081

Çam, M., Kuşcu, I., & Kaymakci, N. (2018). An epithermal Au mineralization within a dextral strike-slip deformation corridor; Karadere low sulfidation epithermal deposit (Balıkesir-Turkey). *Geophysical Research. Abstracts*, *20*, EGU2018–8057-1.

Collins, W. J. (2002). Nature of extensional accretionary orogens. *Tectonics*, *21*(4), 1258–1272. https://doi.org/10.1029/2000TC001272

Colquhoun, G. P., Hughes, K. S., Deyssing, L., Ballard, J. C., Folkes, C. B, Phillips, G., Troedson, A. L., & Fitzherbert, J. A. (2025). *New South Wales Seamless Geology dataset, version 2.5 [Digital Dataset]*. Geological Survey of New South Wales, Department of Primary Industries and Regional Development, Maitland.

Corbett, G. (2012). *Controls to low sulphidation epithermal Au–Ag mineralisation*. Presentation to Sydney Mineral Exploration Discussion Group (SMEG).

Dong, G., Morrison, G., & Jaireth, S. (1995). Quartz textures in epithermal veins, Queensland—Classification, origin and implications. *Economic Geology*, *90*(6), 1841–1856. https://doi.org/10.2113/gsecongeo.90.6.1841

Downes, P. M., Tilley, D. B., Fitzherbert, J., & Clissold, M. E. (2016). Regional metamorphism and the alteration response to selected Silurian to Devonian mineral systems in the Nymagee area, Central Lachlan Orogen, New South Wales—A HyLogger™ case study. *Australian Journal of Earth Sciences*, *63*(8), 1027–1052. https://doi.org/10.1080/08120099.2016.1259183

Dube, B., Mercier-Langevin, P., Kjarsgaard, I., Hannington, M., Becu, V., Cote, J., Moorhead, J., Legault, M., & Bedard, N. (2014). The Bousquet 2-Dumagami world-class Archean Au-rich volcanogenic massive sulfide deposit, Abitibi, Quebec: Metamorphosed submarine advanced argillic alteration footprint and genesis. *Economic Geology*, *109*(1), 121–166. https://doi.org/10.2113/econgeo.109.1.121

Duerden, P. (2010). The McPhillamys gold deposit, a significant discovery in the Lachlan Fold Belt, central western NSW. In *Mineral exploration in the Tasmanides, Mines and Wines 2010* (pp. 1–16). AIG Bulletin 52.

Fergusson, C. L., & Colquhoun, G. P. (2021). Devonian–Carboniferous regional deformation in the northeastern Lachlan Orogen, southeastern Australia. *Australian Journal of Earth Sciences*, *68*(8), 1092–1110. https://doi.org/10.1080/08120099.2021.1898467

Fitzherbert, J. A., Montgomery, K., Eastlake, M., & Downes, P. M. (2024). What is the McPhillamys orebody? Characteristics and the question of genesis. CWEDG presentation, *Geological Survey of New South Wales reports* (GS2025/0010).

French, T., Duerden, P., Bigelow, J., Simmons, H., & Flitcroft, P. (2015). The McPhillamys gold deposit, Kings Plains, NSW, discovery history and geology of the McPhillamys gold deposit, Lachlan Fold Belt, NSW. In *Mineral exploration in the Tasmanides, Mines and Wines 2015* (pp. 69–73). Australian Institute of Geoscientists 62.

French, T., Duerden, P., Simmons, H., & Flitcroft, P. (2017). McPhillamys gold deposit. In N. Phillips (Ed.), *Australian ore deposits* (pp. 759–762). Australasian Institute of Mining and Metallurgy 32.

Glen, R. A., Walshe, J. L., Bouffler, M., Ho, T., & Dean, J. A. (1995). Syn and post-tectonic mineralisation in the Woodlawn deposit, New South Wales, Australia. *Economic Geology*, *90*(6), 1857–1864. https://doi.org/10.2113/gsecongeo.90.6.1857

Glen, R. A., & Watkins, J. J. (1994). The Orange 1:100 000 Sheet: A preliminary account of stratigraphy, structure and tectonics, and implications for mineralisation. *Geological Survey of New South Wales, Quarterly Notes*, *95*, 1–17.

Glen, R. A., & Watkins, J. J. (1999). Implications of Middle Devonian deformation of the eastern part of the Hill End Trough, Lachlan Orogen, New South Wales. *Australian Journal of Earth Sciences*, *46*(1), 35–52. https://doi.org/10.1046/j.1440-0952.1999.00687.x

Goldfarb, R. J., Baker, T., Dubé, B., Groves, D. I., Hart, C. J. R., & Gosselin, P. (2005). Distribution, character, and genesis of gold deposits in metamorphic terranes. In J. W. Hedenquist, J. F. H. Thompson, R. J. Goldfarb & J. P.

Richards (Eds.), *Economic geology 100th anniversary volume* (pp. 407–450). Society of Economic Geologists. https://doi.org/10.5382/AV100.14

Goldfarb, R., & Groves, D. (2015). Orogenic gold: Common or evolving fluid and metal sources through time. *Lithos*, *233*, 2–26. https://doi.org/10.1016/j.lithos.2015.07.011

Green, D., & Schodlok, M. (2016). Characterisation of carbonate minerals from hyperspectral TIR scanning using features at 14 000 and 11 300 nm. *Australian Journal of Earth Sciences*, *63*(8), 1–7. https://doi.org/10.1080/08120099.2016.1225601

Hedenquist, J. W., Aribas, A., & Gonzalez-Urien, E. (2000). Exploration for epithermal gold deposits. In S. G. Hagemann & P. E. Brown (Eds.), *Gold in 2000. Reviews in economic geology, 13* (pp. 245–277). Society of Economic Geologists. https://doi.org/10.5382/Rev.13.07

Henley, R. W. (1985). The geothermal framework of epithermal deposits. In B. R. Berger & P. M. Bethke (Eds.), *Geology and geochemistry of epithermal systems reviews in economic geology* (Vol. 2, pp. 1–24). Society of Economic Geologists.

Henry, C. D., Elson, H. B., McIntosh, W. C., Heizler, M. T., & Castor, S. B. (1997). Brief duration of hydrothermal activity at Round Mountain Nevada, determined from $^{40}Ar/^{39}Ar$ geochronology. *Economic Geology*, *92*(7-8), 807–826. https://doi.org/10.2113/gsecongeo.92.7-8.807

Hughes, K., & Fitzherbert, J. A. (2025). *Thermal infrared characterisation of carbonate minerals in drill core from the McPhillamys Gold project*. Geological Survey of New South Wales Report.

Huston, D. L., Champion, D. C., Mernagh, T. P., Downes, P. M., Jones, P., Carr, G., Forster, D., & David, V. (2016). Metallogenesis and geodynamics of the Lachlan Orogen: New (and old) insights from spatial and temporal variations in lead isotopes. *Ore Geology Reviews*, *76*, 257–267. https://doi.org/10.1016/j.oregeorev.2015.07.005

Huston, D. L., Champion, D. C., Morrison, G., Mass, R., Thorne, J. P., Carr, G., Beams, S., Bottrill, R., Chang, Z-S., Dhnaram, C., Downe, P. M., Forster, D. B., Gemmell, J. B., Lisitsin, V., McNeill, A., & Vicary, M. (2017). *Spatial variations in lead isotopes, Tasman Element, eastern Australia*. Geoscience Australia Record, 2017 (09). Geoscience Australia.

Li, H., Wang, Q., Yang, L., Dong, C., Weng, W., & Deng, J. (2022). Alteration and mineralization patterns in orogenic gold deposits: Constraints from deposit observation and thermodynamic modelling. *Chemical Geology*, *607*, 121012. https://doi.org/10.1016/j.chemgeo.2022.121012

McCuaig, T. C., & Kerrich, R. (1998). P–T–t–deformation–fluid characteristics of lode gold deposits: Evidence from alteration systematics. *Ore Geology Reviews*, *12*(6), 381–453. https://doi.org/10.1016/S0169-1368(98)00010-9

Morales-Leal, J. E., Menzies, A., Wilke, H. G., & Zuluaga, J. (2022). Characterization and distribution of adularia and other alteration minerals by X-ray diffraction analysis at the El Peñón Au-Ag epithermal deposit, northern Chile. *Andean Geology*, *49*(2), 185–207. https://doi.org/10.5027/andgeoV49n2-3400

Ohmoto, H., & Rye, R. O. (1979). Isotopes of sulfur and carbon. In H. L. Barnes (Ed.), *Geochemistry of hydrothermal ore deposits* (2nd ed., pp. 509–567). John Wiley and Sons.

Oviedo, L., Fuster, N., Tschischow, N., Ribba, L., Zuccone, A., Grez, E., & Aguilar, A. (1991). General geology of La Coipa precious metal deposit,

Atacama, Chile. *Economic Geology*, *86*(6), 1287–1300. https://doi.org/10.2113/gsecongeo.86.6.1287

Packham, G. H. (1999). Radiometric evidence for Middle Devonian inversion of the Hill End Trough, northeast Lachlan Fold Belt. *Australian Journal of Earth Sciences*, *46*(1), 23–33. https://doi.org/10.1046/j.1440-0952.1999.00684.x

Pal, D. C., Barton, M., & Sarangi, A. K. (2009). Deciphering a multistage history affecting U–Cu(–Fe) mineralization in the Singhbhum Shear Zone, eastern India, using pyrite textures and compositions in the Turamdih U–Cu(–Fe) deposit. *Mineralium Deposita*, *44*(1), 61–80. https://doi.org/10.1007/s00126-007-0165-z

Pogson, D. J., & Watkins, J. J. (Comps.) (1998). *Bathurst 1:250 000 geological sheet SI/55-8, explanatory notes*. Geological Survey of New South Wales.

Powell, C. M. (1976). Geology of hill end trough Molong high: A critical appraisal of the tectonic history of the hill end trough and its margins. *Bulletin of the Society for Exploration Geophysicists*, *7*(1), 14–18. https://doi.org/10.1071/EG976014

Powell, C. M., & Edgecombe, D. R. (1978). Mid-Devonian movements in the northeastern Lachlan Fold Belt. *Journal of the Geological Society of Australia*, *25*(3-4), 165–167. https://doi.org/10.1080/00167617808729026

Roche, W. (1889). Bathurst District—Blayney Division. In *Annual report of the Department of Mines, New South Wales for the Year 1888* (pp. 64–65). Department of Mines, New South Wales.

Rhys, D. A., Lewis, P. D., & Rowland, J. V. (2020). Structural controls on ore localisation in epithermal gold-silver deposits: A mineral systems approach. In J. Rowland & D. Rhys (Eds.) *Applied structural geology of or-forming hydrothermal systems. Reviews in economic geology* (Vol. 21, pp. 83–145). Society of Economic Geologists. https://doi.org/10.5382/rev.21.03

Schodlok, M. C., Whitbourn, L. B., Huntington, J. F., Mason, P., Green, A. A., Berman, B., Coward, D., Connor, P., Wright, W., Jolivet, M., & Martinez, R. (2016). HyLogger-3, a visible to shortwave and thermal infrared reflectance spectrometer system for drill core logging: Functional description. *Australian Journal of Earth Sciences*, *63*(8), 929–940. https://doi.org/10.1080/08120099.2016.1231133

Simmons, S. F., & Browne, P. R. L. (2000). Hydrothermal minerals and precious metals in the Broadlands–Ohaaki geothermal system: Implications for understanding low-sulfidation epithermal environments. *Economic Geology*, *95*(5), 971–999. https://doi.org/10.2113/95.5.971

Simmons, S. F., Mauk, J. L., & Simpson, M. P. (2000). The mineral products of boiling in the Golden Cross epithermal deposit. *New Zealand Minerals & Mining Conference Proceedings*, *29–31 October 2000.*

Simpson, M. P., & Christie, A. B. (2019). Hydrothermal alteration mineralogical footprints for New Zealand epithermal Au–Ag deposits. *New Zealand Journal of Geology and Geophysics*, *62*(4), 483–512. https://doi.org/10.1080/00288306.2019.1577278

White, N. C., & Hedenquist, J. W. (1995). Epithermal gold deposits: Styles, characteristics and exploration. *SEG Discovery*, *23*(23), 1–13. https://doi.org/10.5382/SEGnews.1995-23.fea

Zhao, S-R., Yu, X-H., Li, J-W., Jiang, S-Y., Wu, Y-F., Zhao, X-F., & L, Z-K. (2023). Early Mesozoic orogenic gold mineralization in the North Qinling Terrane: Insights from rutile U–Pb, mica and K-feldspar $^{40}Ar/^{39}Ar$, and H–O–S–Pb isotopes of the Yangxie gold deposit. *Ore Geology Reviews*, *159*, 105539. https://doi.org/10.1016/j.oregeorev.2023.105539